Crystallization of dipolar particles in two dimensions

Sara Al Jawhari

UNIVERSITÉ DE LORRAINE

École Doctorale SESAMES - Lorraine

THÈSE DE DOCTORAT

Présentée pour obtenir le grade de docteur de
l'Université de Lorraine

Spécialité: Physique

CRYSTALLIZATION OF DIPOLAR PARTICLES IN TWO DIMENSIONS

par

SARA AL JAWHARI

Soutenue le 13 Octobre 2015 devant le jury composé de :

Nicolas Vandewalle	Pr, Université de Liege	Examinateur
Hervé Mohrbach	Pr, Université de Lorraine	Président
Catherine Quilliet	MCF, Université Joseph Fourier	Rapporteur
Hendrik Meyer	CR, Université de Strasbourg	Rapporteur
Lydiane Bécu	MCF, Université de Lorraine	Co-directeur de thèse
René Messina	Pr, Université de Lorraine- Metz	Directeur de thèse

ICPM - 1 bd Arago, Technopôle, 57070 Metz, France

Tel : +33 (0)3 87 54 73 98 www.lcp-a2mc.univ-lorraine.fr/

Acknowledgment

If I were to thank everyone that contributed to my success, this acknowledgements section would exceed the length of this thesis work Many thanks are in order... First on the list is my director Prof. Rene Messina, his knowledge and enthusiasm were my driving force to be where I am right now. I realized that because of the pressure Rene puts on me I was capable of achieving more than expected. I would also like to thank my co-director MCF. Lydiane Becu for her continuous support, starting with the administrative work while I was in Lebanon ending with all the social and academic advice she gave from the moment I reached the lab. Also With the help of Lydiane I was able to conduct the experimental part of this thesis. In addition I am so grateful to Lahcen Assoud for the fruitful discussion we had through out the binary mixtures part of this thesis work. Thanks also to GRASP group under the direction of Prof. Nicolas Vandewalle in Université de Liege for the nice cooperation we had for the first part of the thesis. I would also like to thank the members of the lab LCP-A2MC for their kind reception and treatment during my stay here, namely the director of the lab Pr. Olivier Pages and colleagues Rami Haj Hussein, Osman Alwan, Juliana Srour and Osman Kahraman. Special thanks go to the members of the Jury,the directors and responsibles in ecole doctorale SESAMES for their institutional support throughout these academic years. Alaa Alhariri,Ekbal Alzoubi,Wahida Handouzi,Hayat Daod,Amina lazrak,Wafa Ghnimi,Delal Dridi,Ahmed baker,thank you for helping me to survive these 3 years experience, without your existence my friends I think passing this work would be more difficult. My family, whatever I do I can not thank you enough ...you lighted up my road with your entire spiritual and financial support patience and unconditional love.

Finally, I wouldn't have made it through out this thesis without my husband Adel Harb, thanks for always being there for me day by day with all your encouragement, patience and love...

Abstract

This thesis deals with two-dimensional crystallization of dipolar particles. The first part of the manuscript treats one component systems. There, the idea of using excited dry granular media as substitutes of wet colloidal suspensions is exploited to tackle the problem of crystallization. Athermal two-dimensional granular systems are exposed to external mechanical noise leading to Brownian-like motion. Using tunable repulsive interparticle interaction via an external imposed magnetic field, it is shown that the same microstructure as that observed in colloidal suspensions can be quantitatively recovered at a macroscopic scale. To that end, experiments on granular (realized by the GRASP group in Liège) and colloidal systems made up of magnetized particles as well as computer simulations are performed and compared. Excellent agreement throughout the range of the dipolar coupling is found for the pair distribution as well as the bond-orientational correlation functions. This finding opens new ways to efficiently and very conveniently explore phase transitions, crystallization, nucleation, etc in confined geometries. The second part of this thesis addresses two component systems. Binary mixtures made up of particles carrying similar dipole moments are investigated. Using Monte Carlo simulations, a detailed structural analysis based on partial pair distribution functions and microstructure snapshots is presented for high dipolar coupling. At equimolar composition, the relevance of the coexistence of triangular superlattices with stoichiometry AB_2 and A_2B is revealed, with $A(B)$ standing for the large(small) dipole moments. This finding is in excellent qualitative agreement with the zero temperature theoretical predictions.

Résumé

Cette thèse porte sur la cristallisation bidimensionnelle de particules dipolaires. La première partie concerne les systèmes à un composant. L'idée d'utiliser des matériaux granulaires *secs* comme substituts de suspensions colloïdales *mouillées* y est exploitée pour aborder le phénomène de cristallisation. Des systèmes granulaires athermaux bidimensionnels sont alors exposés à un bruit mécanique extérieur conduisant à un mouvement de type brownien des grains. En utilisant des interactions interparticulaires répulsives via un champ magnétique externe imposé, on montre que la microstructure observée dans les suspensions colloïdales peut être retrouvée quantitativement à l'échelle macroscopique. A cette fin, des expériences sur des granulaires (réalisées au laboratoire GRASP à Liège) et sur des systèmes colloïdaux constitués de particules magnétiques ainsi que des simulations numériques sont effectuées et comparées. Un excellent accord pour toute la gamme de couplage dipolaire est obtenu pour les fonctions de distribution de paires ainsi que pour les fonctions de corrélation orientationnelles. Cette découverte ouvre de nouvelles possibilités pour explorer efficacement et aisément les transitions de phase, la cristallisation, la nucléation, etc. dans des géométries confinées. Le second volet de cette thèse concerne les systèmes à deux composants. Des mélanges binaires constitués de particules pourvues de moments dipolaires similaires sont examinés. En utilisant des simulations Monte Carlo, une analyse structurale détaillée basée sur les fonctions de distribution de paires partielles et les clichés de microstructures est présentée pour un couplage dipolaire fort. Pour une composition équimolaire, la coexistence entre des super-réseaux triangulaires avec une stoechiométrie AB_2 et A_2B est mise en évidence, où $A(B)$ dénote les grands (faibles) moments dipolaires. Ce résultat est en très bonne adéquation avec les prédictions théoriques à température nulle.

List of Publications

The work described in this thesis has been published in the following papers:

1. René Messina, Sarah Aljawhari, Lydiane Bécu, Julien Schockmel, Geoffroy Lumay and Nicolas Vandewalle.
   Quantitatively mimicking wet colloidal suspensions with dry granular media *Nature. Scientific Reports,* ***5****:10348, 2015*

2. René Messina, Sarah Aljawhari.
   Crystallization of binary mixtures with similar dipole moments in two dimensions (submitted to EPL).

Conference Participation:

Poster communication:
Sarah Aljawhari, Lydiane Bécu, René Messina, Julien Schockmel, Geoffroy Lumay and Nicolas Vandewalle.

Crystallization of granular magnetic particles in two dimensions.
9^{th} *Liquid Matter Conference 2014* Lisbon, 21-25 July 2014.

URL: http://www.fc.ul.pt/en/conferencia/liquids-2014

Contents

Introduction

This thesis deals with crystallization in two dimensions of dipolar particles. In particular, we study the case where particles are characterized by a typical size belonging to the so-called *mesoscopic* scale, which ranges from 1 nm to 1 μm (see figure 1). Such systems are called *Colloids* and are ubiquitous in everyday life: for example milk (fat globules dispersed in a water-based fluid), blood (red blood cells suspended in plasma) and paint (pigments suspended in solvent) are all systems composed of colloidal particles.

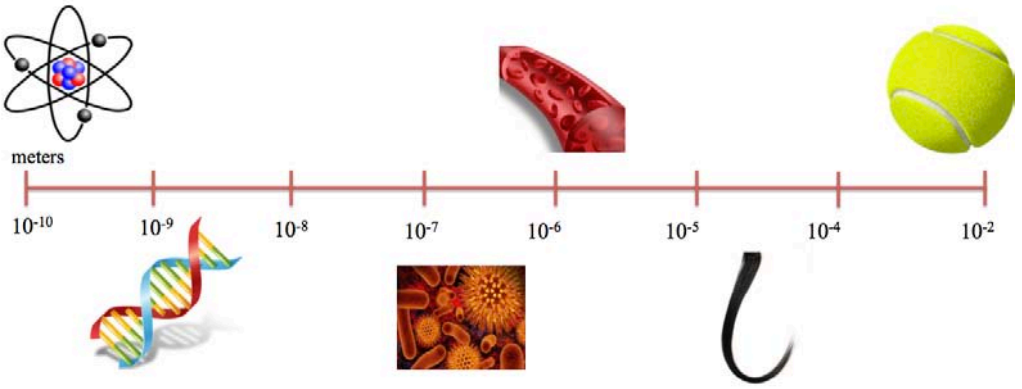

Figure 1 – A length scale ruler showing different particles size from atomic to macroscopic scale. Starting from left to right the pictures refers to: Atom($\sim 10^{-10}$ m), DNA strand($\sim 10^{-9}$ m), H1N1 viruse particles($\sim\ 10^{-7}$ m), red blood cells($\sim\ 10^{-6}$ m), human hair ($\sim 10^{-4}$ m), tennis ball ($\sim 10^{-2}$ m).

The scientific field known as colloidal science has been initiated by the Scottish chemist Thomas Graham in 1861, who observed that compared to molecular solutes, mesoscopic-sized particles exhibited slower diffusion times [1]. This discovery implied that the so-called colloids are larger than atoms, but yet not large enough to be seen by the naked eye. An essential characteristic of colloidal particles is that they are subjected to Brownian motion, originating from the thermal energy of order of k_BT. This foundation was credited to Brown [2].

Colloidal particles are sufficiently small to display properties similar to those

of atomic systems. In particular, theories known from statistical mechanics can be applied for both systems [3]. However, comparatively to atomic systems, colloidal systems offer an easy visualisation of their structure with optical methods and the interaction between particles can be easily tuned. This analogy between colloids and atomic systems has proved particularly useful for the study of crystallization [4, 5], where colloidal suspensions have being used as powerful model systems. Crystallization and more generally phase transitions constitute a central topic in condensed matter physics [4, 6]. It plays a fundamental role in fabrication of crystalline materials and, therefore, is of great importance for many applications. In particular, colloidal crystals [7] are of great interest for developing photonic bandgap materials [8] or optical filters [9] that form by self-assembly. Images of binary crystals demonstrating the crystallisation phenomenon occuring at different typical length scales are displayed figure 2.

In two dimensions, Peierls [13] and Mermin [14] have shown that long-range translational order does not exist at finite temperature. Thus, crystallisation features may depend on the dimensionality. In the 80s, the formation of two-dimensional colloidal crystals was observed experimentally with hardcore like interparticle interactions [15, 16], with charged particles [17], and with so-called magnetic holes [18]. In parallel, computer simulations were carried out as well to explore the solid phase behavior of two dimensional systems, e.g. hard disks [19], soft Lennard-Jones spheres [20, 21], and a one component plasma [22]. There has been a long debate on the possible existence of the predicted Kosterlitz- Thouless- Halperin-Nelson-Young (KTHNY) melting process [23–25], mediated by topological defects in a two dimensional solid. This theory predicts a two-stage melting scenario where an intermediate phase in the transition from solid to liquid phase sets in, namely the so-called *hexatic* phase. During the solid-hexatic transition, the long-ranged translational order is lost but the orientational one persists, whereas the longe-ranged orientational order vanishes during the hexatic-liquid transition. This theory was successfully confirmed experimentally in the late 90s by the Maret's group, who was able to develop a new experimental setup allowing a comprehensive study of the two dimensional phase transitions [26–29]. A simplified scheme of their experimental setup is sketched in figure 3.

A major achievement of this thesis (see Chapter 2) was to quantitatively mimic *wet micron-sized colloids* with *dry millimeter-sized* particles (granular media) [31]. In the same spirit of the experiment depicted in figure 3, an external magnetic field was used to tune the interparticle repulsive dipolar interaction enabling a quantitative microstructure comparison between both systems. To that end, athermal granu-

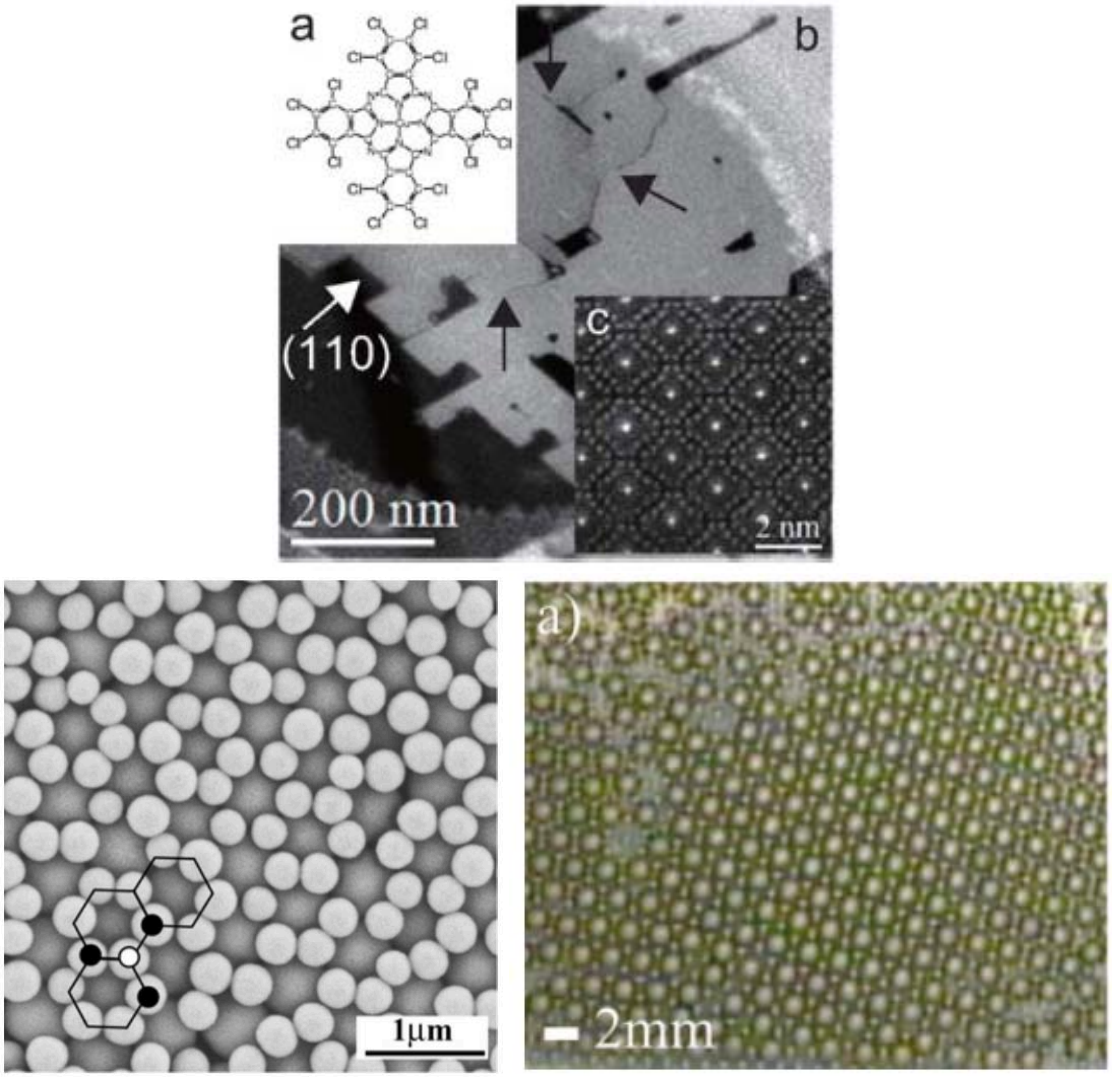

Figure 2 – Binary crystals at different scales, the macroscopic, mesoscopic and atomistic level. The pictures from left to right refers to: binary granular system [10], colloidal binary AB_2 crystalline structure [11], $Cl_{16}CuPc$ molecular crystal [12].

lar systems were excited by an external mechanical noise leading to Brownian-like motion. [1] Moreover computer simulations were performed to corroborate these experimental findings.

The other central task of this thesis was devoted to two component systems, see Chapter 3. It is well known that binary mixtures present a much richer variety of solid phases than their one-component counterpart. In this study, Monte Carlo simulations are employed to explore the phase behavior of binary mixtures made up of similar dipole moments at high dipolar coupling. Indeed an important question

1. The experiments on granular media were performed by the GRASP Laboratory of Liège [32].

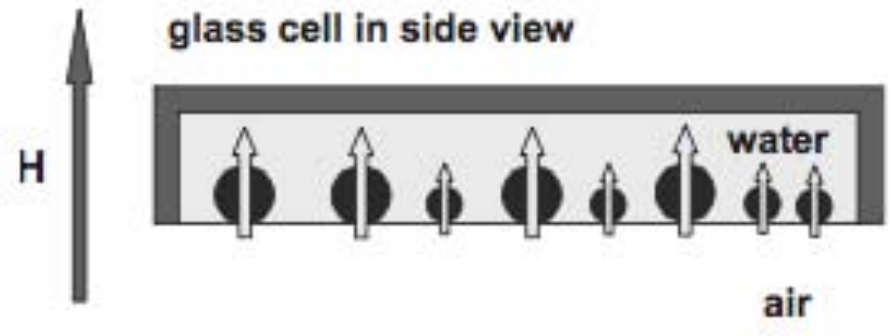

Figure 3 – Scheme of the Maret's group experimental setup [30]. Superparamagnetic particles are confined by gravity on a water/air interface created by a pending drop. An external magnetic field is applied to induce a dipole moment in the particles leading to repulsive pair interactions varying like $1/r^3$.

remains to be answered: what are the coexisting crystal structures in that regime of similar dipole moments at equimolar composition?

The organization of this thesis will follow the outline given below:

— Chapter 1 is devoted to the methods used in our experiments and computer simulations. The relevant orders parameters are also introduced there.

— In Chapter 2, a quantitative comparison of the two-dimensional crystallization taking place (i) in horizontally vibrated granular media and (ii) in colloidal monolayers is presented.

— Chapter 3 deals with the phase behavior of binary mixtures made up of similar dipole moments at high dipolar coupling.

— Conclusions and perspectives are gathered at the end of the manuscript.

Chapter 1

Methods

1.1 System and Experimental Tools

1.1.1 Colloidal suspension of super-paramagnetic spheres

1.1.1.1 Super-paramagnetic spheres and their magnetic moment

Life technologies enterprise provided the colloidal particles for our experiments [33]. The beads are uniform spherical super-paramagnetic of diameter 4.5μm suspended in distilled water, see Fig. 1.1.

According to the information provided by the enterprise, Dynabeads® magnetic beads are uniform, non-porous, super-paramagnetic, mono-dispersed and highly cross-linked polystyrene microspheres consisting of an even dispersion of magnetic material throughout the beads. The magnetic material within the Dynabeads® consists of a mixture of maghemite ($\gamma - Fe_2O_3$) and magnetite (Fe_3O_4). The iron content (Fe) of the beads is 20% by weight in Dynabeads® M-450 epoxy. The magnetic beads are coated with a thin polystyrene shell which encases the magnetic material, and prevents any leakage from the beads or trapping of ligands inside the bead. Due to the doping with iron oxide, applying an external magnetic field $\vec{B}$ induces a magnetic moment $\vec{m}(B)$ which is parallel to the field, and depends on the magnitude of the magnetic field. These 4.5 μm microspheres display a super-paramagnetic behavior [1]. The field created at a point $\vec{r}$ by a magnetic dipole moment

1. Super-paramagnetism is a form of magnetism, which appears in small ferromagnetic or ferrimagnetic nanoparticles. In sufficiently small nanoparticles, magnetization can randomly flip direction under the influence of temperature. The typical time between two flips is called the Néel relaxation time. In the absence of an external magnetic field, when the time used to measure the magnetization of the nanoparticles is much longer than the Néel relaxation time, their magnetization appears to be in average zero: they are said to be in the super-paramagnetic state. In this state, an external magnetic field is able to magnetize the nanoparticles, similarly to a paramagnet. However, their magnetic susceptibility is much larger than that of paramagnets.

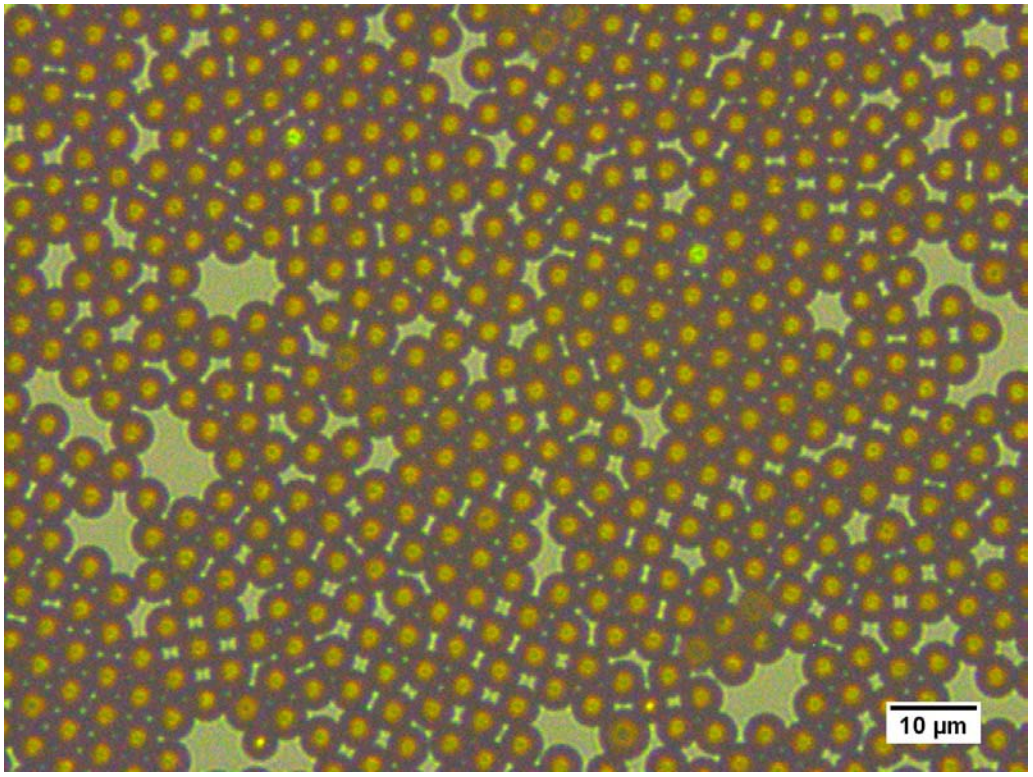

Figure 1.1 – A concentrated raw sample of Dynabeads with lens objective × 50.

$\vec{m}$ located at the origin of the frame of reference is given by :

$$\vec{B} = \frac{\mu_0}{4\pi} \frac{3(\vec{r}.\vec{m})\vec{r} - r^2\vec{m}}{r^5} \tag{1.1}$$

The interaction energy U between two dipoles $\vec{m_1}$ and $\vec{m_2}$ is given by the magnetic field $\vec{B_2}$ created by dipole $\vec{m_2}$ and the position of dipole $\vec{m_1}$ and can be expressed by $U = -\vec{m_1}.\vec{B_2}$. Using Eq. 1.1 this can be written as:

$$U = -\frac{\mu_0}{4\pi} \frac{3(\vec{r}.\vec{m_1})(\vec{r}.\vec{m_2}) - r^2\vec{m_1}.\vec{m_2}}{r^5} \tag{1.2}$$

where $\vec{r}$ represents the position vector between the two dipoles. Since the magnetic field $\vec{B}$ is homogeneous, the two magnetic dipoles are equal. Substituting $\vec{m_1} = \vec{m_2} = \vec{m}$ in Eq. 1.2 this gives:

$$U = \frac{\mu_0}{4\pi} \frac{r^2m^2 - 3(\vec{r}.\vec{m})^2}{r^5} \tag{1.3}$$

For two particles placed along the field line the relation $\vec{r}.\vec{m} = rm$, leads to $U = -2\mu_0 m^2/4\pi r^3$, therefore two particles located on the same field line attract.

Oppositely in the case where the particles are placed in a plane perpendicular to that of the magnetic field $\vec{B}$ (which is our case) $\vec{r}.\vec{m} = 0$. This leads to a repulsive dipole-dipole interaction with final expression:

$$U = \frac{\mu_0}{4\pi}\frac{m^2}{r^3} \tag{1.4}$$

For a super-paramagnetic particle the magnetic dipole moment is defined by the Langevin function:

$$m(B) = m_0 L(\alpha B) \qquad L(x) = coth(x) - \frac{1}{x}, \tag{1.5}$$

where m_0 denotes a saturation moment and the constant α represents the inverse of the typical field necessary to reach saturation. For small values of the magnetic field $\vec{B}$ it is possible to linearise Eq. 1.5 to obtain:

$$m(B) = \frac{1}{3} m_0 \alpha B = \chi_m B, \tag{1.6}$$

where χ_m is the magnetic susceptibility of the Dynabeads. The determination of the magnetic susceptibility is usually done by magnetophoresis experiments [34–36]which were not performed on our batch of Dynabeads. Since we used the same type of magnetic particles as in [27], we can infer that the susceptibility should be very similar. The values determined in [26] were $\chi_m = (7.3 \pm 0.9).10^{-11} Am^2/T$, $m_0 = (5.7 \pm 0.4).10^{-13} Am^2$ and $\alpha = (3.9 \pm 0.4).100\ T^{-1}$. With these values one can plot the magnetic moment of the particles as function of the magnetic field $\vec{B}$ see Fig. 1.2. Before ending this section we would like to discuss the possible particle interactions in the absence of a magnetic field. The Debye screening length, κ^{-1}, is calculated from the definition:

$$\kappa^2 = \frac{2e^2 N_A C}{10^3 \epsilon k_B T}. \tag{1.7}$$

In Eq. 1.7 e is the charge of electron, N_A is Avogadro's number, k_B is the Boltzmann constant, T is the temperature, ϵ is the solvent dielectric constant, and C is the concentration in mol/L. By adding 7.28×10^{-3} mol/L of surfactant SDS (Sodium dodecyl sulfate), the Debye length is found to be 3.6 nm, and therefore one can exclude the effects due to electrostatic repulsions. Although Van der Waals forces are important at short distance as they lead to aggregation of particles if the solution is not stabilized by adding surfactant, their influence is negligible for the given separating distance of the particles. Moreover a weak magnetic field causes a gap

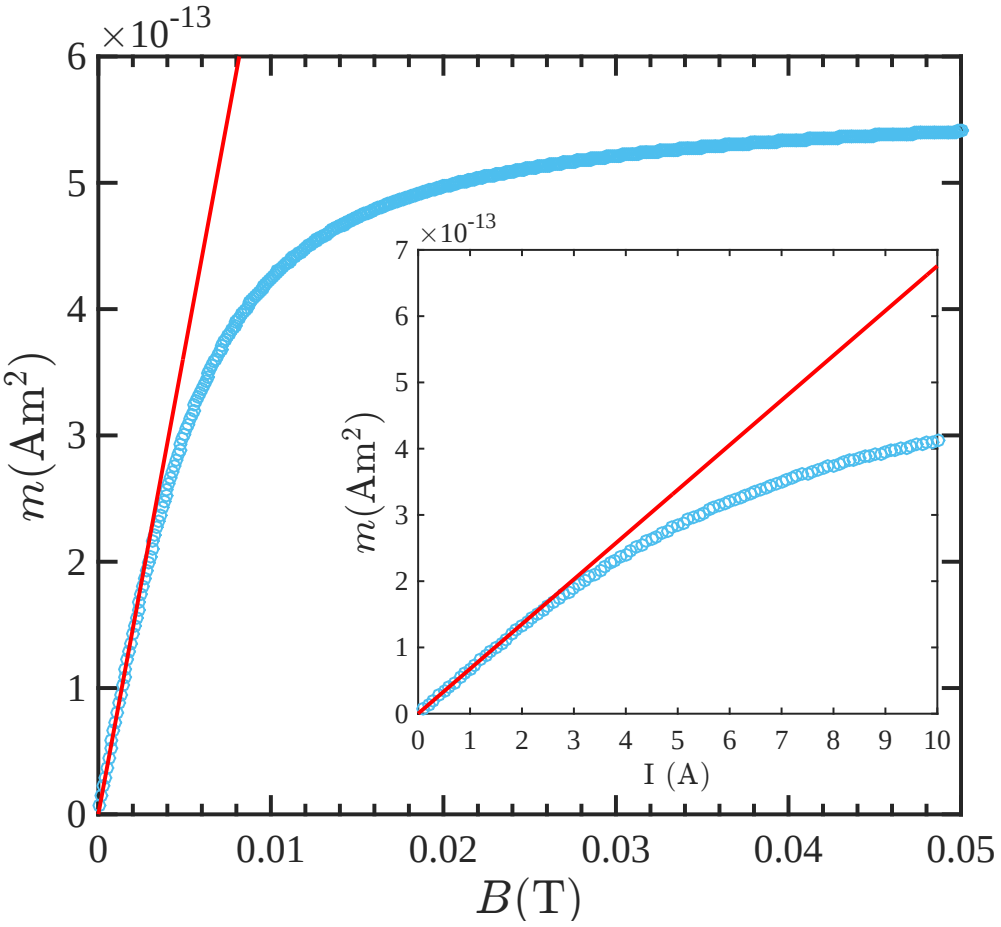

Figure 1.2 – Representation of the magnetic moment of our particles as function of the magnetic field B. The relation becomes non-linear for high values of B as deduced from the deviation from the straight red line. The inset shows the magnetic moment as function of the applied current I.

between two spheres which shows that the Van der Waals attraction is negligible compared to the magnetic interaction. So, with the possible effects of electrostatic repulsion and Van der Waals being neglected, the system's only contributing interaction is the magnetic repulsive interaction given by Eq.1.4.

Finally we introduce the coupling parameter Γ which represents the ratio of the magnetic energy to the thermal energy k_BT of two particles at a distance $1/\sqrt{\rho}$, where ρ is the particle number density.

$$\Gamma = \frac{\mu_0}{4\pi}\frac{m^2\rho^{3/2}}{k_BT} = \frac{\mu_0}{4\pi}\frac{\chi_m^2 B^2\rho^{3/2}}{K_BT}. \tag{1.8}$$

In all that follows, Γ will always be used to describe the interaction energy for a given set of particles.

1.1.1.2 Preparation of the colloidal suspension

For this experimental study we found that a careful sample preparation procedure was extremely necessary before beginning our series of measurements. We noticed that the beads tend to aggregate in pure distilled water as shown in Fig. 1.3. To avoid this problem the addition of a surfactant sodium dodecyl sulfate (SDS)

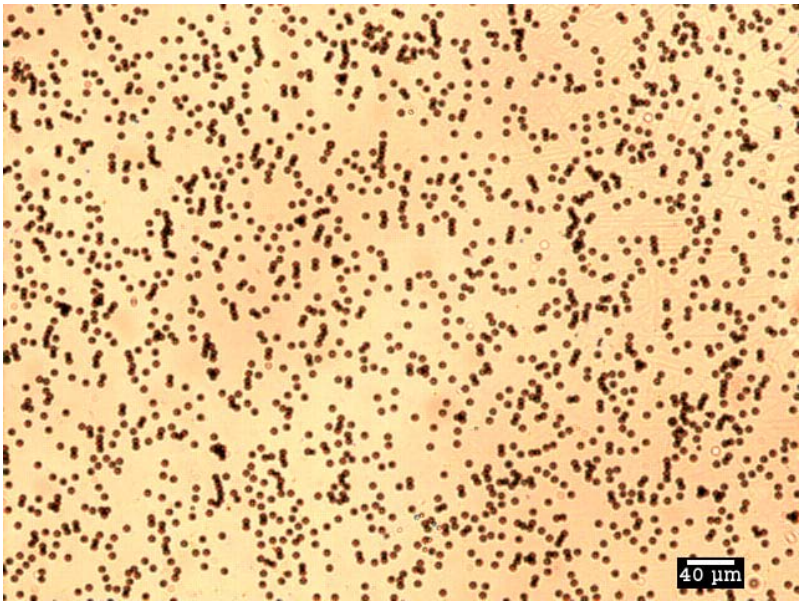

Figure 1.3 – Microscope snapshot taken with objective $\times 10$ showing chains formation when particles are suspended in pure distilled water

of concentration slightly less than the critical micelle concentration (CMC) was needed (about 2.1g/l-2.2g/l). However the suspension still contained some pair of aggregates (doublets). Sonication of the sample just before using it was the only way to break the doublets and obtain a suspension exclusively constituted of non aggregated particles. In general, short sonication is a good way to reduce aggregation of the beads but with iron inclusions in the beads, more care is needed, as the binding might break. Sonication should not exceed 12 minutes at low amplitude, because the particles will be damaged and thus lose their magnetic properties. A picture of bad sonication trial is shown in Fig. 1.4.

1.1.2 General description of the Experimental Setup

1.1.2.1 Sample holder

Two typical types of cell were used(see Fig. 1.5). They were custom made by fixing a hollow cylinder on a glass slide, using a 2 components epoxy glue which

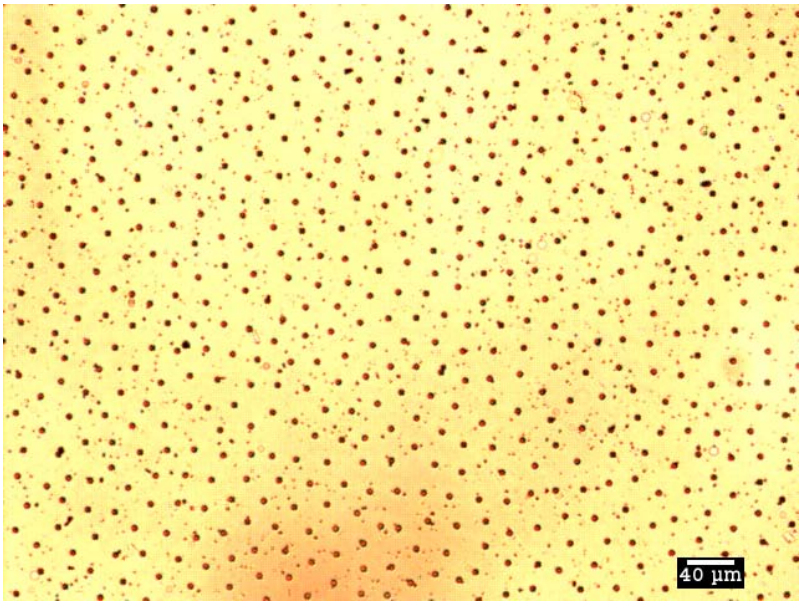

Figure 1.4 – Microscope image showing the results of intense sonication, where the very tiny dots indicate that the particles were broken and lost their iron content and thus their magnetic properties.

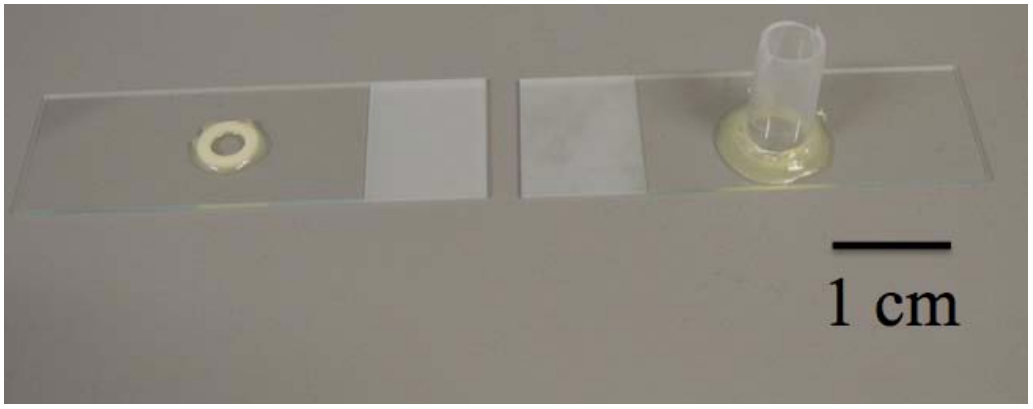

Figure 1.5 – The two typical cells used to conduct these experiments, as shown both cells are glued on a glass slide.

shows no visible interaction with the particles. Bulk concentration is adjusted to keep surface concentration constant. Since the mass density of the colloidal particles is $1.7 \times 10^{-3} kg/m^3$, the particles in suspension are subjected to sedimentation. As a consequence all the particles fall on the glass/water interface and remain confined there due to gravity, thus creating a monolayer on the glass slide. Placing the glass slide on the microscope support we ensure that our system is flat which is necessary to avoid gradients of particle concentration.

Before going on further with the description of the optical part, one should note

that after several trials we notice that the cleanliness of the cell used is extremely important. It is essential to check that the cell is clean before starting our series of measurements. Without these precautions, if the glass slide or the inner part of the cylindrical cell is not completely clean, impurities (see Fig. 1.6) are generally suspended in water and contaminate the interface. The protocol used to clean the

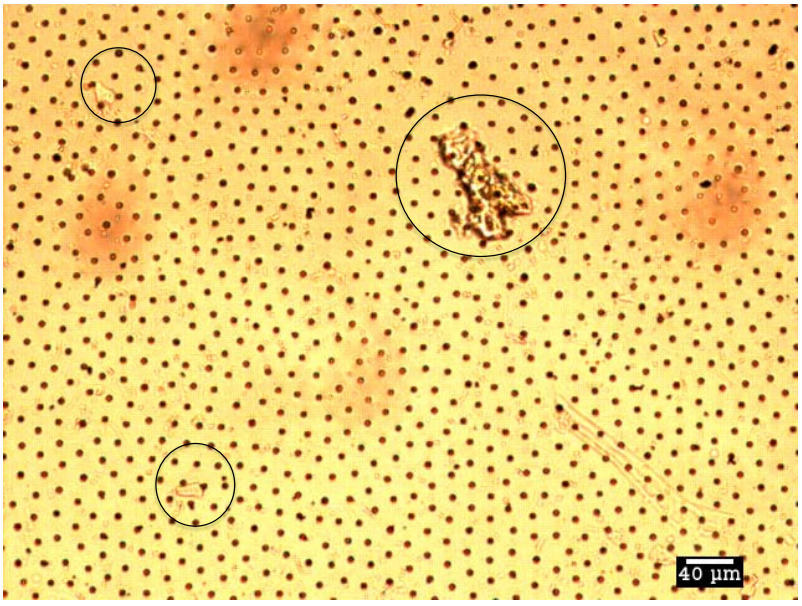

Figure 1.6 – Microscope image showing the impurities that fall on the interface (see encircled objects). The number of impurities keep growing with time as a results of not having a clean cell initially.

cell consists in rinsing the cell with SDS and distilled water for about 30 minutes, and if necessary repeating this process until no impurities can be detected under the microscope. After filling the cell with the suspension, we wait a sufficiently long time to ensure that all beads have sedimented. Failing to do so might lead to the formation of chains of beads upon application of the magnetic field. The external magnetic field is applied in the direction normal to the glass/water interface and leads to a mutual repulsion between the particles. The potential interaction energy (described in section 1.1.1) can be controlled by varying the magnitude of the magnetic field.

1.1.2.2 The external magnetic field $\vec{B}$

The field is considered to be uniform and homogeneous and is generated by a flat coil having a radius $R = 6.5cm$ and length $L = 1.25cm$. The coil has N=95 turns enclosing an area of $1mm^2$ enamelled copper wire. The maximum admissible

current is 5A (7A for a few minutes) which was sufficient to reach the crystalline phase. The induction at the center of the coil is given by the formula:

$$B = \mu_0 I \times 731,$$

where I being the current applied measured by a multimeter. Substituting this expression in Eq.1.6 yields the magnetic moment of our particles as function of I, which is plotted as inset in Fig. 1.2. In the range of current used in our experiments (0 to 4A), this plot shows that we stayed in the linear regime of Eq. 1.5.

1.1.2.3 Optical Device

Visualization of the particles is carried out with an inverted microscopic (Nikon ECLIPSE TI-E) equipped with a GIGE vision Camera(Type Prosilica, GE640 / 640C) (see Fig. 1.7). We could widen or decrease the field of view by changing

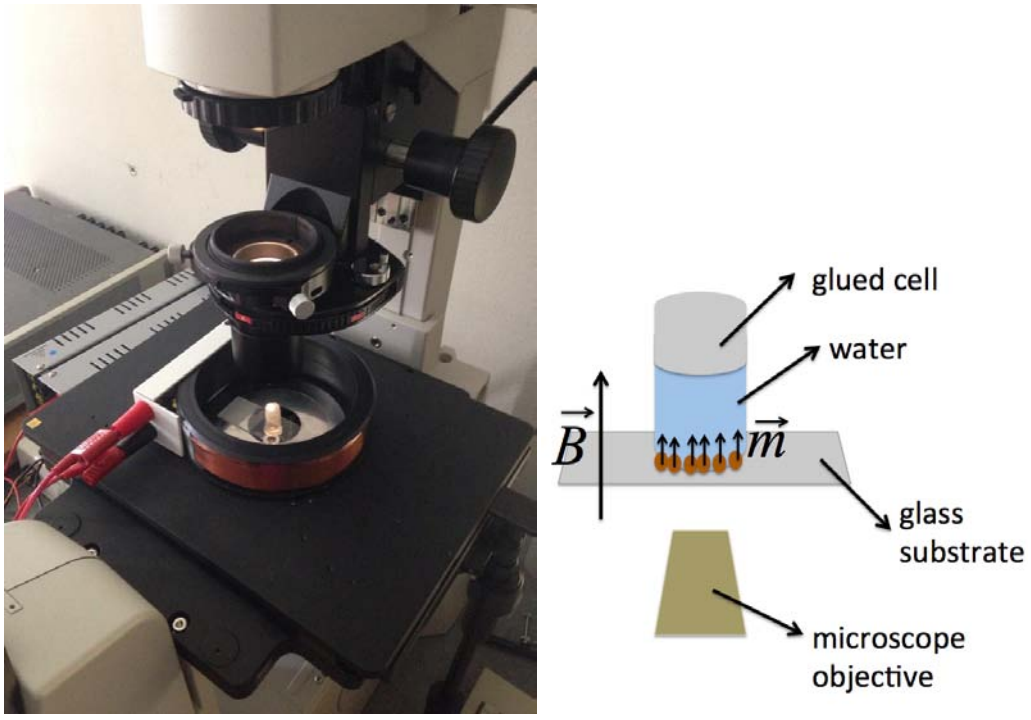

Figure 1.7 – Left panel: A real picture of our device showing the sample placed at the center of the coil. Right panel: A schematic representation of the setup.

the lens objective($5\times, 10\times, 40\times$). The lens $\times 10$ objective was the most suitable one. Typically the field of view is $560 \times 480\ \mu m^2$ containing about 1200 to 1400 particles, with the cell surface area being $7.85 \times 10^{-5} m^2$ the whole sample contains approximately 270000 particles in total. This provided a sufficient number of particles for a good statistical study. The lens objective used (Nikon, plane-achromat, $\times$ 10, ELWD condenser) has a particularly high working length depth, which allowed

us to obtain good image quality through the rather thick glass slide at the bottom of the sample cell. With these conditions images are captured by the camera, processed and then analyzed on a PC. The operating software image analysis will be discussed in the next section.

1.1.2.4 Image Processing

After certain equilibration time, series of images where recorded every 10 s. These images were then processed with the use of *ImageJ* software. The image of resolution 640×480 pixels^2 is first converted to 8-bit black and white image and then adjusted to a certain threshold, see Fig. 1.8. We checked that changing the threshold does not affect at all the statistical properties we are interested in. The particle detection works by scanning the image until it finds the edge of an object. Particles in the image are then selected based on their size in $(pixel^2)$ and circularity (a circularity of 1 indicates a perfectly circular shape). This ensures that only beads are selected by the program. The center of mass of the beads, which is the brightness-weighted average of its x and y coordinates, is then output. It provides the precise coordinates of the center of the beads.

Finally a plug-in script is written to treat a batch of images and extract the coordinates of each bead. The text file containing the positions of the beads was used as an input in a C language program to calculate the structural parameters $g(r)$ and $g_6(r)$.

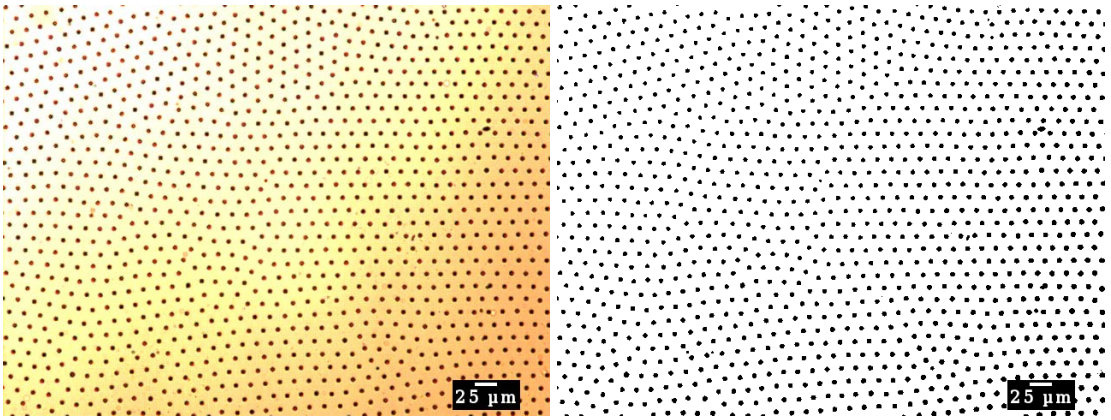

Figure 1.8 – Microscope image of $\sim$ 1300 particles in the field of view of 560×480 μm^2 ($10 \times$ objective). This image corresponds to an interaction strength Γ=32. The left panel corresponds to the real image, whereas the right one corresponds to the thresholded 8-bit grey scale image used to get the coordinates of particles.

1.2 Simulation Methods

1.2.1 Cell Geometry

Inspired by the cell geometry of the experimental granular materials [32], our starting configuration was built the same way. A set of N particles (here point-like particles) were arranged in a perfect triangular lattice. In general to fill a triangular lattice confined within a hexagonal cell, N should follow the relation [37]:

$$N = 3p^2 - 3p + 1 \tag{1.9}$$

where p is the number of particles on each outer edge see Fig. 1.9. In our case we used $N = 547$ corresponding to $p = 14$ as an initial hexagonal configuration, as performed by the GRASP group [38] see Fig. 1.9. For a triangular lattice, the nearest neighbour distance between two particles is defined by $b = (\frac{2}{\sqrt{3}\rho})^{1/2}$, with ρ being the particle number density. So the hexagonal cell was built in a way such that the outer radius R_{out} (see Fig. 1.12) of a circumscribed circle around the hexagon can be written in terms of this distance b, with $R_{out} = (p-1)b$.

1.2.2 Monte Carlo Procedure

The Total interaction Potential

In parallel with experiments, we have performed Monte Carlo (MC) computer simulations [39], under constant density and temperature. Mimicking the experiments on granular materials and colloidal suspensions, particles (point-like) are confined in a hexagonal box in two dimensions, in simulation they interact via the pair potential:

$$\frac{U(r_{ij})}{k_B T} = \Gamma \left(\frac{1}{r_{ij}\sqrt{\rho}} \right)^3 \tag{1.10}$$

Γ is the dimensionless coupling parameter defined in Eq. 1.8, r_{ij} is the distance separating two particles i and j. Γ is the only key parameter controlling the interaction strength.

The total energy of the system is the sum of all interactions between pairs of particles and can be expressed by:

$$U_N = \sum_{i>j}^{N} U(r_{ij}). \tag{1.11}$$

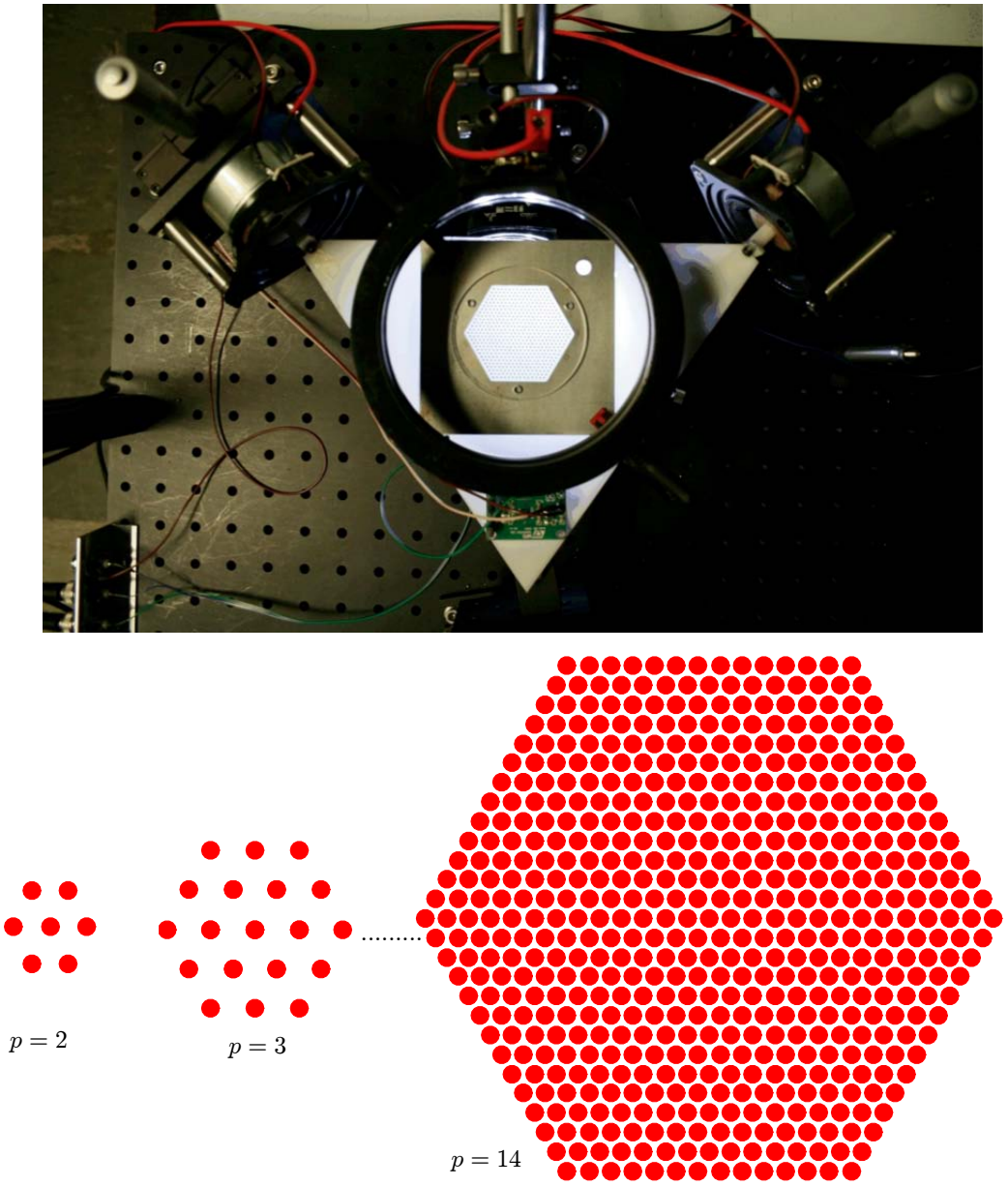

Figure 1.9 – Top panel: top view of the experimental setup for the granular material used by GRASP [38]. Bottom panel: Illustrations of perfect finite triangular lattices enclosed in a hexagonal cell for different values of p (see Eq. 1.9).

Relaxation towards equilibrium

The Metropolis algorithm [40] for a single particle move was used. Typically 5×10^6 MC steps were used to equilibrate the system, and additional 5×10^6 MC steps were used to gather statistics for the computation of the required observables. We have carefully checked that upon starting with a perfect lattice or fully randomly generated configuration, identical properties are obtained within the statistical un-

certainties as shall be seen in section 1.3. The energy profile for these two different starting configuration is shown in Fig. 1.10. The fact that the same minimum energy is reached warranties that equilibrium is indeed reached.

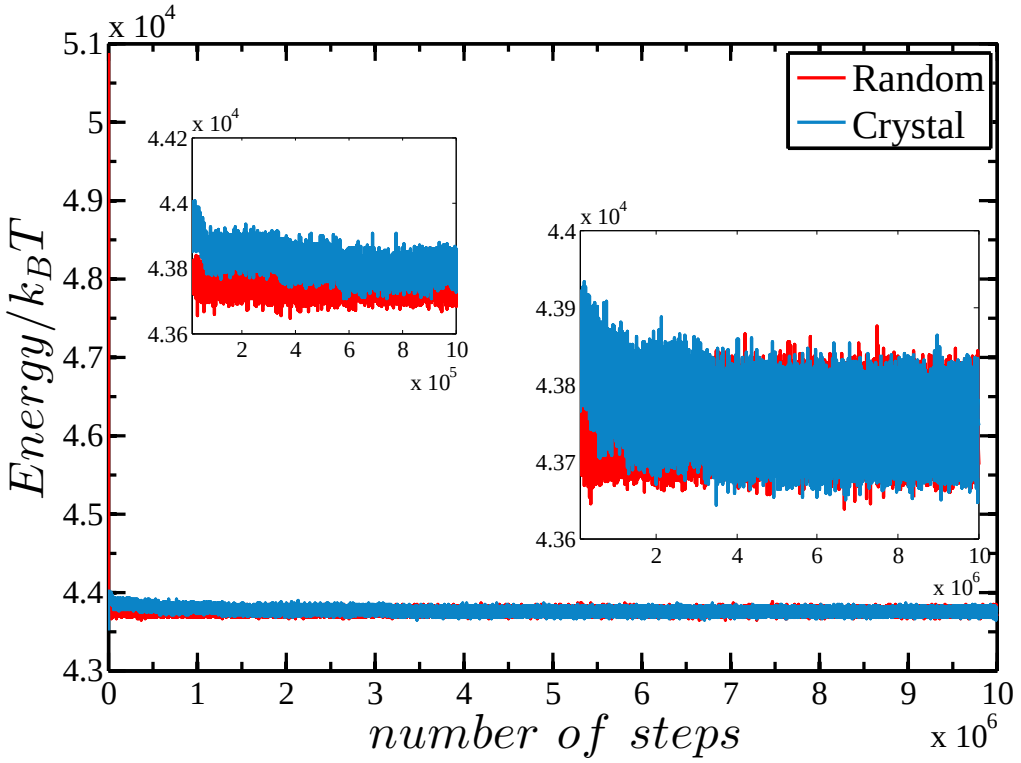

Figure 1.10 – Plot of the energy profile (in k_BT units) of the system comparing the two starting configurations. Red profile corresponds to a random starting distribution, whereas the blue one corresponds to a perfect crystal initial configuration.

1.3 Order Parameters

1.3.1 Pair distribution function

1.3.1.1 Basic formalism for liquid structure

In the canonical ensemble, consider a system of N particles in a constant volume V at temperature T, the probability of finding particle 1 lying between $\vec{r}_1$ and $\vec{r}_1 + d\vec{r}_1$, particle 2 lying between $\vec{r}_2$ and $\vec{r}_2 + d\vec{r}_2$,..., particle N lying between $\vec{r}_N$ and $\vec{r}_N + d\vec{r}_N$ is given by [41]:

$$P^{(N)}(\vec{r_1}...\vec{r_N}) = \frac{\exp[-\beta U_N]}{Z_N} d\vec{r_1}...d\vec{r_N} \tag{1.12}$$

$$\text{with} \qquad Z_N = \int ... \int \exp[-\beta U_N] d\vec{r}_1 ... d\vec{r}_N$$

where Z_N is the so-called configuration integral. $P^{(N)}(\vec{r}_N)$ is normalized in such a way that:

$$\int P^{(N)}(\vec{r}_1 ... \vec{r}_N) d\vec{r}_1 ... d\vec{r}_N = 1$$

$\vec{r}_1 ... \vec{r}_N$ represents an ensemble of coordinates of all N particles, $d\vec{r}_i = dx_i dy_i$, U_N is the total interaction potential energy between the particles defined in the previous section, and $\beta = 1/kT$. One can also define the probability of "reduced" configuration [42] where only portions of the particles are fixed, say n ($n < N$), the corresponding probability is obtained by integrating over the degrees of freedom $\vec{r}_{n+1} ... \vec{r}_N$ leading to:

$$P_N^{(n)}(\vec{r}_1 ... \vec{r}_n) = \frac{1}{Z_N} \int ... \int exp[-\beta U_N] d\vec{r}_{n+1} ... d\vec{r}_N \tag{1.13}$$

Similarly $P_N^{(n)}$ is normalized such that:

$$\int P_N^{(n)}(\vec{r}_1 ... \vec{r}_n) d\vec{r}_1 ... d\vec{r}_n = 1$$

If the particles are non distinguishable, then the probability that *any* particle at r_1 is in dr_1, ..., and *any* particle at r_n is in dr_n, one defines the *n*-particle density as :

$$\rho_N^{(n)}(\vec{r}_1 ... \vec{r}_n) = \frac{N!}{(N-n)!} P_N^{(n)}(\vec{r}_1 ... \vec{r}_n) \tag{1.14}$$

The term $\frac{N!}{(N-n)!}$ in Eq. 1.14 stems from the fact that one could have N possible ways to chose the first particle, $(N-1)$ to chose the 2^{nd} ..., $(N-n+1)$ ways to chose the n^{th} particle. Eq. 1.14 is normalized as follows:

$$\int \rho_N^{(n)}(\vec{r}_1 ... \vec{r}_n) d\vec{r}_1 ... d\vec{r}_n = \frac{N!}{(N-n)!} \tag{1.15}$$

For the special case where $n = 1$, Eq. 1.14 becomes [2]

$$\rho^{(1)}(\vec{r}_1) = \frac{N!}{(N-1)!} P^{(1)}(\vec{r}_1) = N P^{(1)}(\vec{r}_1) \tag{1.16}$$

2. for simplicity the subscript N in Eq. 1.13, 1.14, 1.15 could be omitted and thus $\rho_N^{(n)} = \rho^{(n)}$

It follows from Eq. 1.15 that the normalization for n=1 is given by :

$$\int \rho^{(1)}(\vec{r}_1)d\vec{r}_1 = \frac{N!}{(N-1)!} = N \tag{1.17}$$

In case of homogeneous systems, Eq. 1.17 leads to:

$$\rho^{(1)}(\vec{r}_1) = \frac{N}{V} = \rho \tag{1.18}$$

At this stage, it is insightful to introduce the so-called *n*-particle distribution function $g_N^{(n)}(r_1...r_n)$ [43] related to the *n*-particle density function as :

$$\rho^n g_N^{(n)}(\vec{r}_1...\vec{r}_n) = \rho_N^{(n)}(\vec{r}_1...\vec{r}_n) \tag{1.19}$$

This equation is only valid for a homogeneous system. If the system is isotropic as well as homogeneous, as in our case, the *pair distribution function* $g^{(2)}(\vec{r}_1, \vec{r}_2)$ is only function of the separation distance between the particles $r_{12} = |\vec{r}_2 - \vec{r}_1|$; written simply as $g(r)$ with $r = r_{12}$. Hence from Eq. 1.19 it follows that :

$$g(r) = \rho^{(2)}(r)/\rho^2 \tag{1.20}$$

Statistical mechanics of fluids [44] shows that $\rho^{(2)}(r)$ is given by:

$$\rho^{(2)}(r) = \left\langle \sum_{i=1}^{N} \sum_{\substack{j=1 \\ i \neq j}}^{N} \delta(r - r_{ij}) \right\rangle$$

Hence, the final expression of the pair distribution function for a homogeneous system can be given by [43]:

$$\rho g(r) = \frac{1}{N} \left\langle \sum_{i=1}^{N} \sum_{\substack{j=1 \\ i \neq j}}^{N} \delta(r - r_{ij}) \right\rangle, \tag{1.21}$$

In two dimensional systems, this is normalized as follows:

$$\rho \int g(r) 2\pi r dr = N - 1, \tag{1.22}$$

indicating that $g(r)$ represents the probability of finding a particle at a distance r from a reference particle [3]. The pair distribution function $g(r)$ is of particular

3. in case of large system, $N - 1 \approx N$ in Eq.1.22

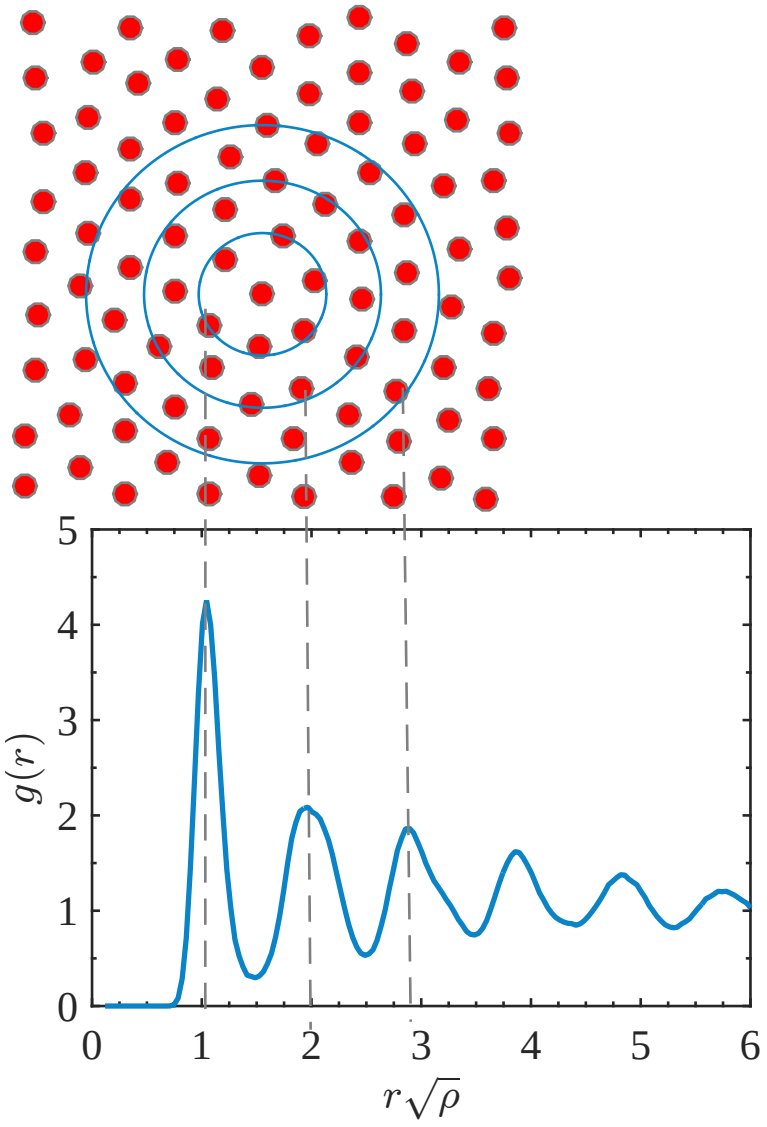

Figure 1.11 – Profile of a typical g(r) establishing the 3 first peaks and the distances between nearest neighbours.

importance, as it is directly related via a Fourier transform to the structure factor of the system, that can be determined experimentally using X-ray diffraction and neutron scattering [45–47]. On the other hand, it is possible, if the particles interact with a pair potential, to express the thermodynamic properties of the system as integrals of the function $g(r)$. An illustrative scheme explaining the meaning of $g(r)$ is shown in Fig. 1.11.

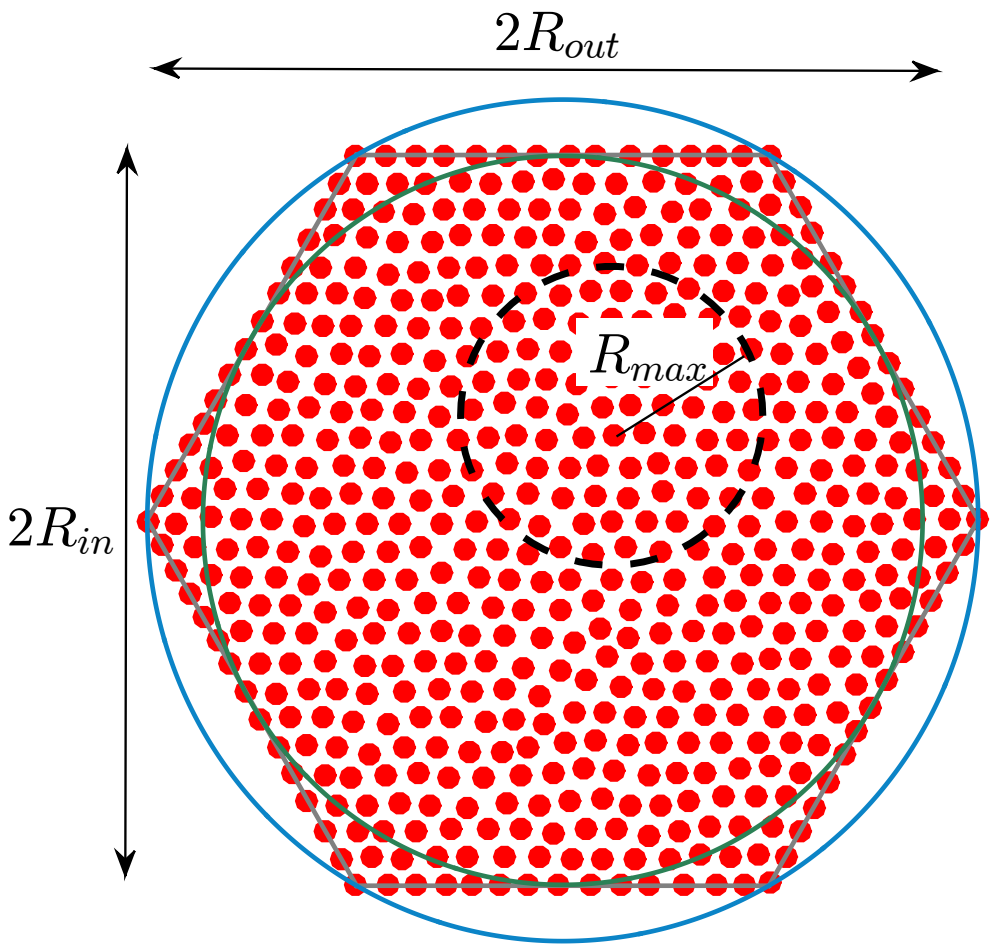

Figure 1.12 – Illustrative figure of computation of $g(r)$. The number of particles N chosen is the number included within a circle of maximum radius R_{max}. R_{max} is half the value of the radius of inner circle (green circle) inscribed in the hexagon with $R_{in} = \sqrt{3}R_{out}/2$, where R_{out} is the outer radius of the blue circle circumscribing the hexagon.

1.3.1.2 Computing the pair distribution function g(r) of a cell geometry

The implementation of our algorithm differs from some previously used methods and it is worth paying them a careful attention. Often to avoid errors due to edge/size effects, the evaluation function around each particle i is limited to a distance r less than a maximum cutoff radius distance R_{max} which we take to be half the radius of the inner circle inscribed inside the hexagon $R_{max} = R_{in}/2$ (Fig. 1.12). Thus each particle explores the same environment as neighboring particles and effects at the edges of the image are excluded. So ρ here is assumed to be a scanned density or effective density and equal to $\frac{N_k}{A}$ where N_k is the number of particles included within an area $A = \pi R_{max}^2$. One might think that because of this

procedure, the correlation function may depend on the value of R_{max}. Indeed, the correlations in Fig. 1.13 do not show a significant dependence on the value of R_{max} chosen. The function g(r) will always be normalized by multiplying the x-axis by

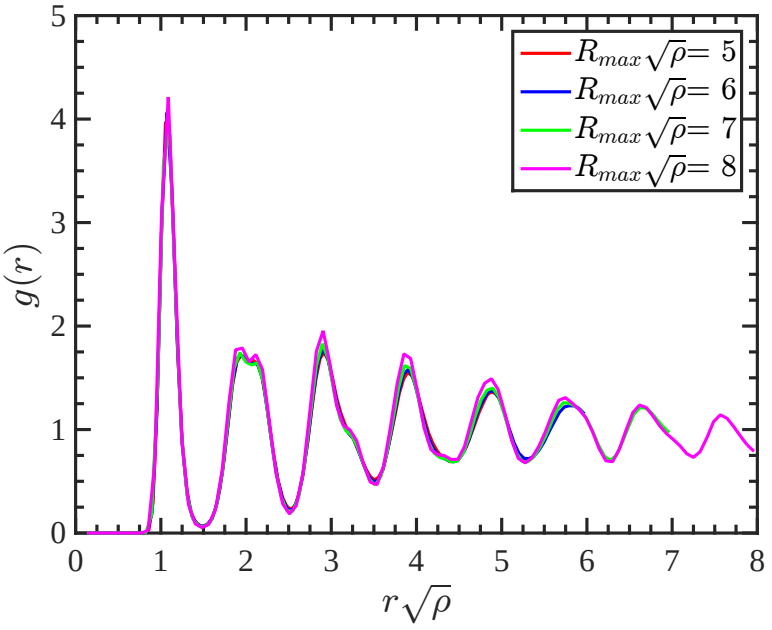

Figure 1.13 – Profiles of the pair distribution function $g(r)$ for different cutoff radii R_{max} at $\Gamma = 21$.

$\sqrt{\rho}$. For a square lattice $1/\sqrt{\rho}$ in fact corresponds to the nearest neighbour distance between the particles and thus g(r) takes its first maximum at a value of about 1. However, for a triangular lattice, the first nearest distance between particles is equal to $b = (\frac{2}{\sqrt{3}\rho})^{1/2}$. The first maximum of g(r) is at a value of about $r = 1.075$.

1.3.1.3 Equilibration and finite size effect check

As discussed before in section 1.2.2, we have carefully checked that equilibrium is attained upon starting from a perfect crystal or starting from a random particles arrangement. We performed a similar check for the pair distribution function $g(r)$ and noticed that they are eventually identical for $N = 547$, see Fig. 1.15.
In addition we have checked finite size effects by varying the hexagonal box size from 547 to 2611 particles, so that according to the relation in Eq. 1.9, the number of layers p is varied from 14 to 30 see Fig. 1.14. The same structural properties given by the pair distribution function (Fig. 1.16) were obtained for large enough cells (hence from $N = 1141$).

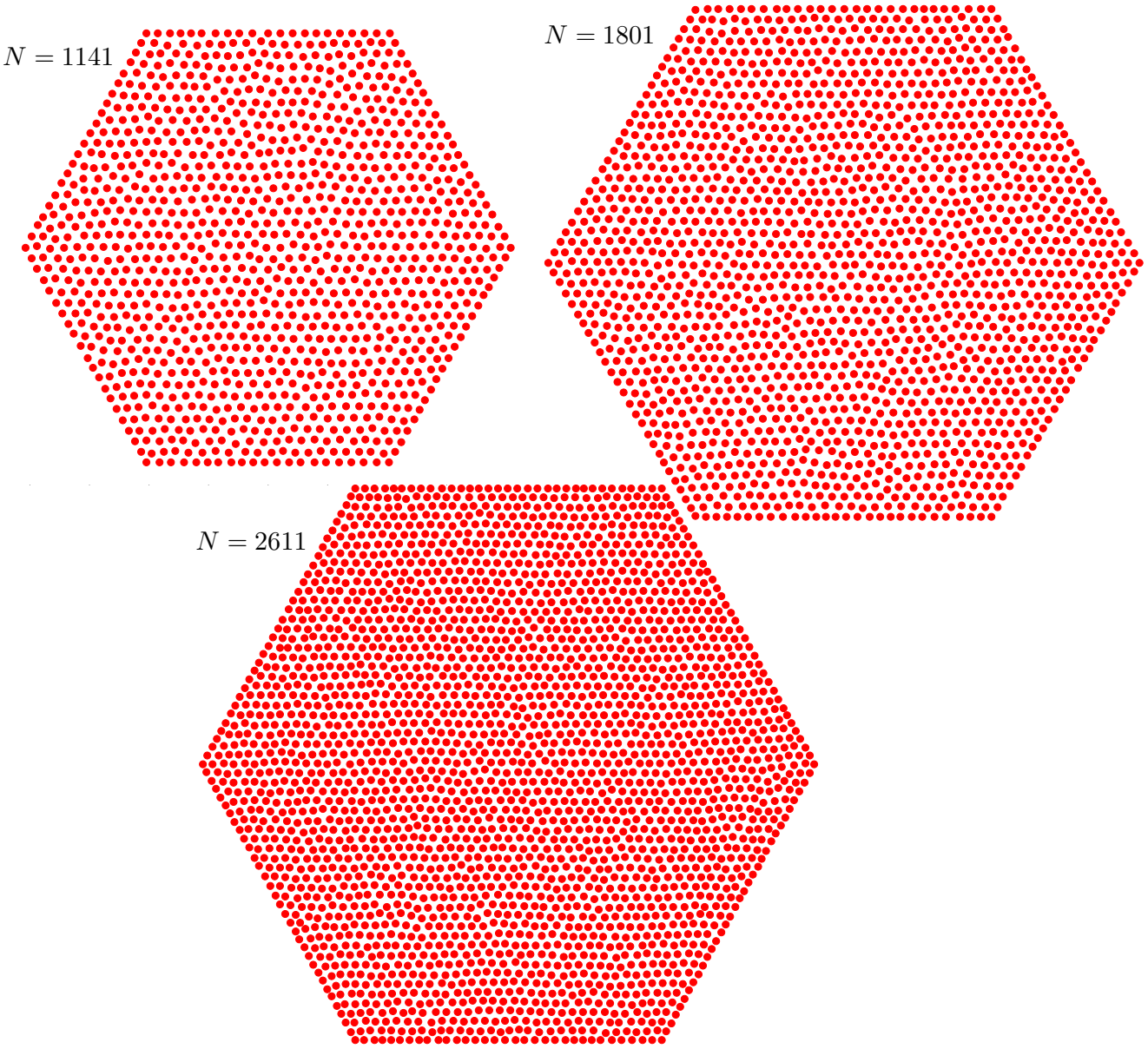

Figure 1.14 – Snapshots at equilibrium at $\Gamma = 21$ for the three different simulation cell sizes that were used to check the size effect problem.

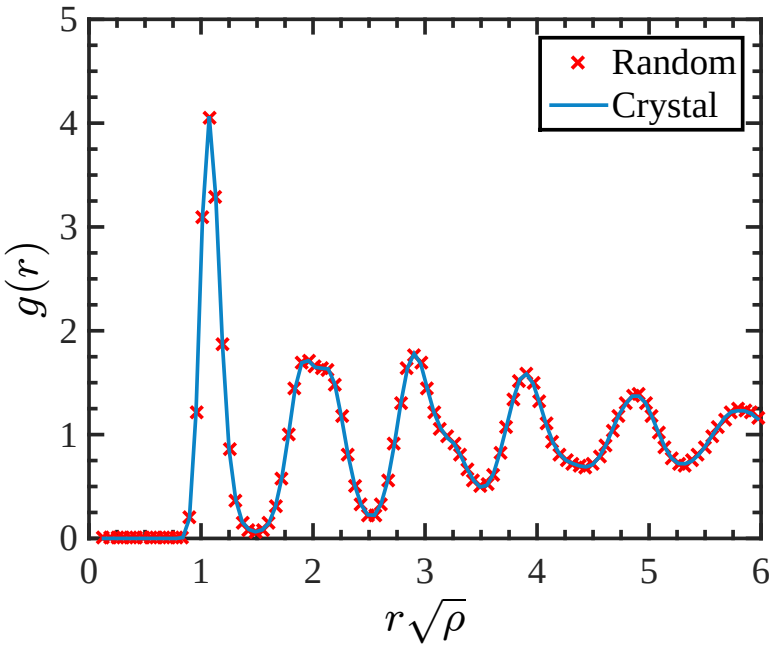

Figure 1.15 – Pair distribution functions for $\Gamma = 21$ with two different starting configurations. The red profile corresponds to initially randomly distributed particles, while the blue one corresponds to an initial perfect crystal .

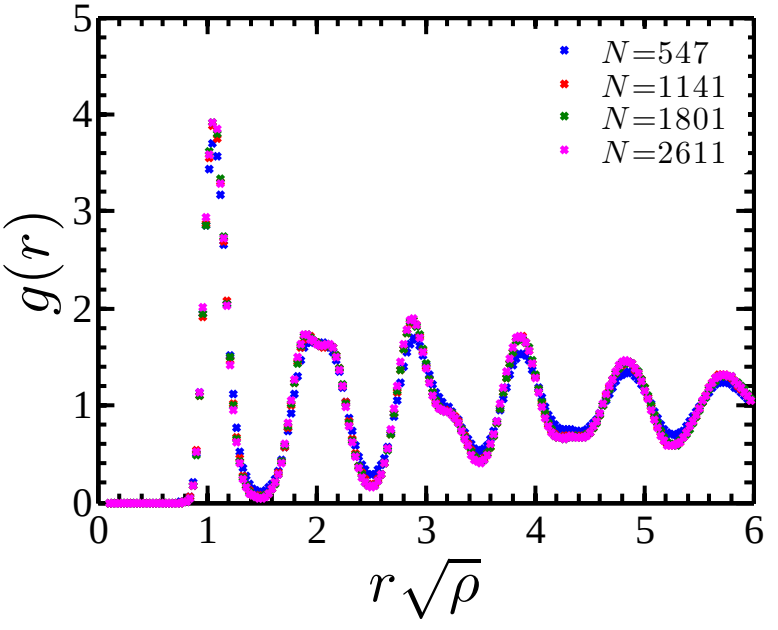

Figure 1.16 – Pair distribution function profiles for different cell sizes at $\Gamma = 21$, ranging from $N = 547$ to $N = 2611$.

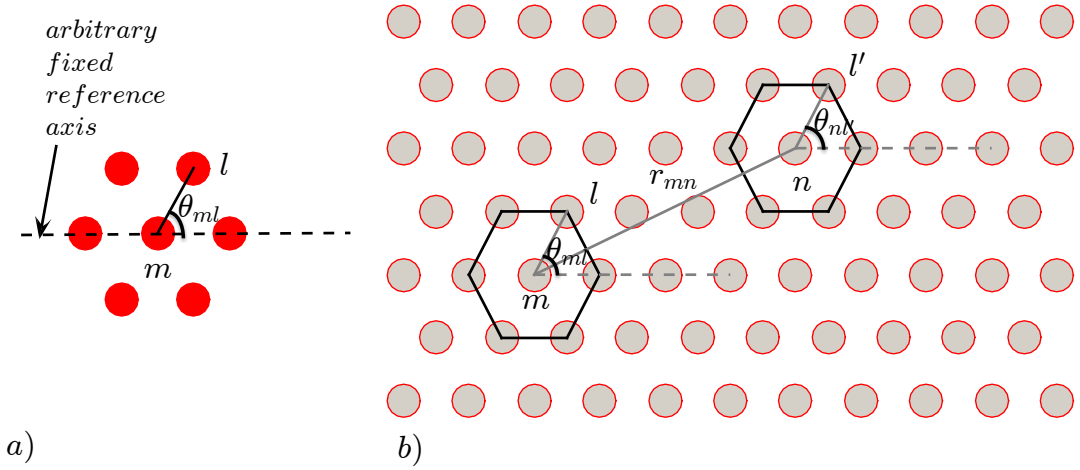

Figure 1.17 – A geometrical sketch for the calculation of the bond orientational correlation function $g_6(r_m - r_n)$ between two particles m and n. Figure (a) illustrates the arbitrary reference axis as well as ml bonds relative to a reference particle m. Figure (b) illustrates two bonds ml and nl' relative to reference particle m and n respectively, which intervene in the calculation of g_6 (see Eq. 2.4).

1.3.2 Bond orientational correlation function $g_6(r)$

1.3.2.1 General definitions

For a perfect triangular lattice each particle is surrounded by six neighbours defining six local bonds, see Fig. 1.17 b. In this zero-temperature situation, all the bond orientations for two different reference particles are identical. In the other limiting case of high temperature, the relative orientation between the bonds of two reference particles are fully uncorrelated. In general, at finite temperature one can quantify the degree of correlation between two bonds of two particles located at $\vec{r}_m$ and $\vec{r}_n$ by introducing the so called *bond orientational correlation function*, which is defined as follows [48] :

$$g_6(r = |\vec{r}_m - \vec{r}_n|) = \langle \psi_6^*(\vec{r}_m)\psi_6(\vec{r}_n)\rangle \tag{1.23}$$

where $\langle ...\rangle$ corresponds to ensemble average. $\psi_6(r_m)$ is the 6-fold *local* bond order parameter at position $\vec{r_m}$, and can be defined as :

$$\psi_6(\vec{r}_m) = \frac{1}{N_m}\sum_{l=1}^{N_m} e^{i6\theta_{ml}} \tag{1.24}$$

where N_m is the number of nearest neighbours of particle m and θ_{ml} is the angle formed between the bond linking particles m and l and an arbitrary prescribed reference axis, a figure explaining this parameter is shown in Fig. 1.17 a. The criterion for choosing nearest neighbors is based on the first minimum of the pair distribution function $g(r)$.

For a perfect triangular lattice, θ_{ml} is a multiple of $\pi/3$ for all m particles. The local bond order parameter $\psi_6(\vec{r}_m)$ is therefore unity for all the particles. Nevertheless, for a non-zero thermal agitation $\|\psi_6\|$ may vary from 0 to unity because of relative change of orientation between particles.

1.3.2.2 Equilibrium and finite size effect check

Like we did for the pair distribution function discussed in section 1.3, the bond orientational correlation function $g_6(r)$ shows also identical properties if one starts with a perfect crystal or random particle distribution see Fig. 1.18. Finite size effect was also checked concerning the orientational order function, Fig. 1.19 shows no significant effect for having large enough cells.

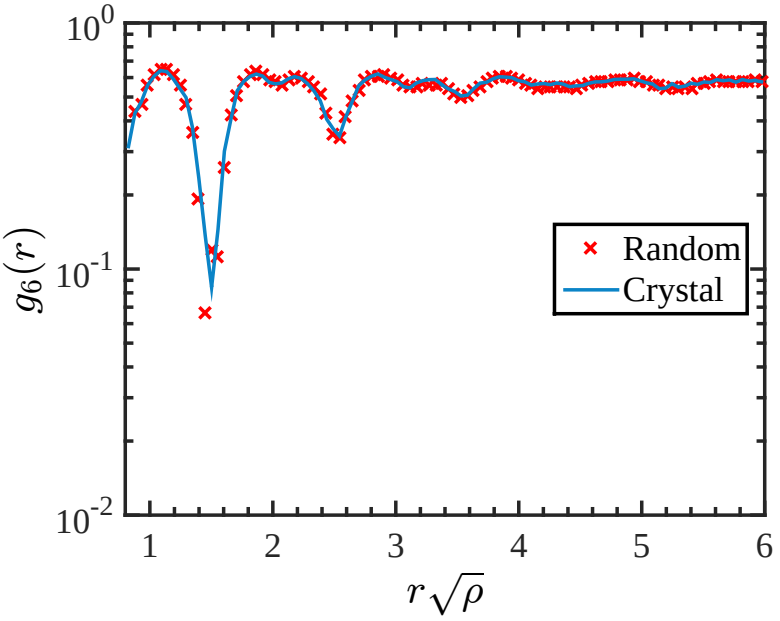

Figure 1.18 – Bond orientational correlation function $g_6(r)$ at $\Gamma = 21$ with two different starting configurations. The red correspond to initially randomly distributed particles, while the blue one corresponds to an initial perfect crystal.

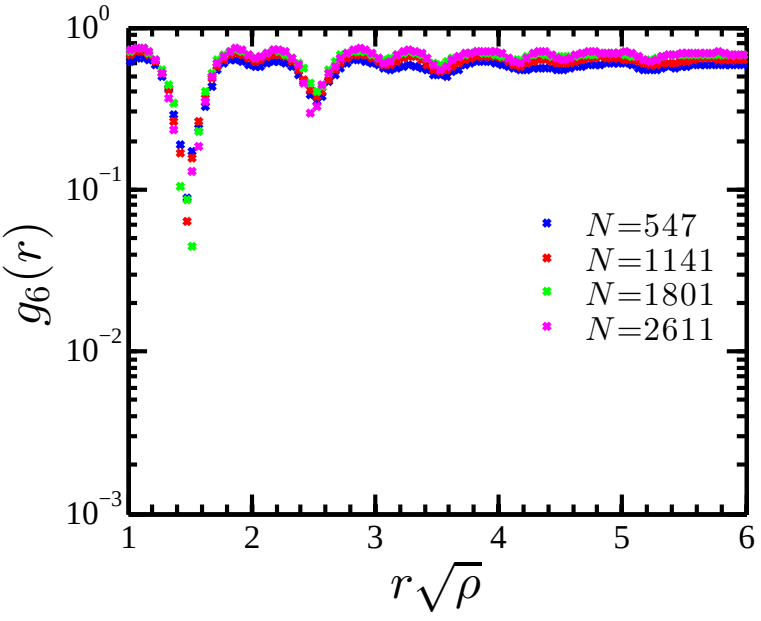

Figure 1.19 – Bond orientational correlation function $g_6(r)$ for different box sizes at $\Gamma = 21$, ranging from $N = 547$ to $N = 2611$.

Chapter 2

Quantitatively mimicking wet colloidal suspensions with dry granular systems

2.1 Introduction

Order vs disorder in condensed matter is a fundamental aspect governing macroscopic properties [49–51]. In this respect, colloidal suspensions represent a model system for the physicist that enables easy visualization of microstructures in the real space, establishing a direct link with the pair potential of the constituting particles. A nice illustration is provided by magnetic monolayers thoroughly studied the two last decades [27,28,52–54]. Thereby ordering and crystallization in two dimensions were investigated experimentally and corroborated by computer simulations when thermal agitation k_BT competes with the particle potential energy U.

At first sight, granular systems made up of *macroscopic* particles possess similarities with colloidal ones. The crucial difference, however, is that thermal fluctuations are negligible for such materials. Hence granular systems are intrinsically *athermal*. Nonetheless, shaking granulates lying on vibrating substrates is a common practice to study two dimensional phase transitions [55–58].

In the present study, GRASP [38] employ a recently proposed technique allowing a precise measurable *induced effective temperature* in two dimensional granular systems [32]. A monolayer of spherical grains is placed within a hexagonal cell which is mechanically shaken in the lateral directions, as sketched in Fig.2.1(a) and (b). By means of Helmholtz coils, see Fig.2.1 (a), an external magnetic field

is applied to induce repulsive interactions between neighboring particles, leading to some ordering of the grains. The mechanical agitation provides a Maxwellian distribution of the velocities of the particles as shown in Fig.2.1(c). The remarkable achievement of this study [32] was thus to establish a bridge between average particle kinetic energy $\langle \frac{1}{2}mv^2 \rangle$ and some effective granular temperature.

One of the goals of this thesis is to show that the same ordering observed in delicate *wet* colloidal suspensions can be advantageously quantitatively obtained with *dry* granular systems that are much easier to manipulate. To accomplish this challenge, we will compare the experimental data of granular systems to those obtained with colloidal systems, as well as numerical Monte Carlo simulations.

2.2 Methods

Granular media

A set of N soft-ferromagnetic beads of diameter 1 mm is confined in a 2D hexagonal cell of diameter 3 cm. The hexagonal cell is shaken horizontally by two loudspeakers oriented in two orthogonal directions (see Fig. 2.1). This mechanical agitation leads to an erratic motion of each beads in the plane. The system is placed in a vertical and homogeneous external magnetic field $\vec{B}$. Considering that each bead has the same dipolar moment $\vec{m}$, the beads interact via a repulsive pair potential

$$U(r_{ij}) = \frac{\mu_0}{4\pi} \frac{\chi_{eff}^2 B^2}{r_{ij}^3}, \tag{2.1}$$

with μ_0 denoting the vacuum permeability and χ_{eff} the effective susceptibility relating the dipolar moment of one bead with $\vec{B}$ such that $\vec{m} = \chi_{eff}\vec{B}$. The interaction is well controlled by adjusting the external magnetic field strength. More specifically by defining $U_m = U(r = 1/\sqrt{\rho})$, with ρ standing for the particle area density, the magnetic coupling can be fully characterized by the dimensionless Γ parameter given by Eq.1.8. In order to obtain reproducible initial conditions, beads are placed in a perfect hexagonal configuration. In order to form a finite triangular lattice, the number of beads N must satisfy the relation $N = 3p^2 - 3p + 1$ where p is the number of beads per outer edge. A special technique was developed by Liege [32] to obtain this perfect arrangement initially. A mask was used of the size and shape of the cell. This mask has an array of holes whose diameter is 30% larger than the diameter of the beads. The system is prepared by placing a bead into each hole of the mask, which then deposited in the cell. Then turning on the external magnetic field

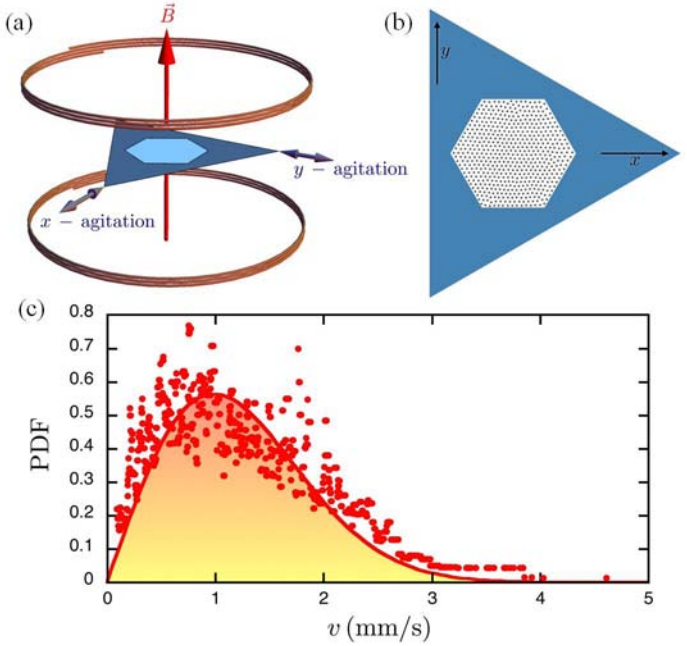

Figure 2.1 – (a) Sketch of the experimental setup for dry macroscopic grains. Millimetric grains of mass m are placed in a hexagonal cell at the center of Helmholtz coils. The vertical field B provides a pair interaction between particles. Two shakers are able to agitate the system along x and y axes. (b) Top view of the cell with typical pattern. (c) The Probability Distribution Function (PDF) of particle velocities v obtained for a fixed low magnetic field. The solid line represents the corresponding Maxwellian distribution [32].

to cause repulsion between the beads. Finally, the mask is removed and repulsion between the beads allows them to keep the organization defined by their position within the mask. It may happen that the beads are glued to the mask, so a countermask is used to remove each ball from its hole. Such process requires a certain precision of execution, so the crystal obtained once the mask is removed, presents few defects. Such technique provides a crystal with fewer defects than those obtained by the method of annealing [59]. This makes the initial conditions for each measurement identical. Such process is also much faster than it seems: the system is prepared in less than ten minutes. The experiment is performed here with N = 547 beads ($p = 14$). Before each measurement, the agitation and the external magnetic field are switched on for 200 seconds to allow the system to reach the equilibrium state. After this initialization process, a CCD camera records a series of images at a fixed rate of 10 frames per second during 100 seconds. A basic tracking method allows one to determine the position and the trajectory of each bead during the whole experiment. Observables are computed from these trajectories, see [32] for details.

Colloidal suspensions

Superparamagnetic colloids of diameter 4.5 μm and mass density 1.7×10^3 kg/m^3 (Invitrogen) are dispersed in a Sodium Dodecyl Sulfate solution in order to prevent their aggregation. The suspension is filled in a cylindrical cell of diameter 1 cm glued on a glass slide. A 2D monolayer is obtained by the sedimentation of the particles on the glass/water interface. The large volume of water above the array of particles prevents any drift induced by thermal gradient or disturbance of the air-water interface. Similarly to the experiments in granular media, the repulsive pair potential given by Eq. 2.1 is generated by an external magnetic field applied perpendicularly to the particle layer. The same definition of the typical repulsion at mean separation $U_m = U(r = 1/\sqrt{\rho})$ holds. The magnetic interaction is increased in small steps followed by an equilibration time of several hours. After equilibration the particles coordinates are determined using an inverted microscope equipped with a CCD camera. Typically, the field of view 560×480 μm^2 contains about 1400 particles. More details of the colloidal experimental methods are given in Methods chapter section 1.1.

Monte Carlo simulations

The very same geometry and number of particles intervening in our experiments on granular media are employed in our numerical MC simulations. The constitutive (here point-like) particles interact via the pair potential

$$\frac{U(r)}{k_BT} = \Gamma\left(\frac{1}{r\sqrt{\rho}}\right)^3. \tag{2.2}$$

A standard MC procedure is executed to generate a canonical ensemble [39]. Typically 10^6 MC steps are used to equilibrate the system and 10^6 additional MC steps are conducted to gather statistics for the computation of the required observables. We have carefully checked that upon starting with a perfect lattice or a fully randomly generated configuration, identical properties are obtained within the statistical uncertainties. This warranties that equilibrium is indeed reached. The experimental values of the effective susceptibilities χ_{eff} for granular and colloidal systems are deduced from the best matching in $g(r)$ between simulations and experiments similarly to what Zahn *et al* [27] did. More details of the simulation methods are given in Methods chapter section 1.2.

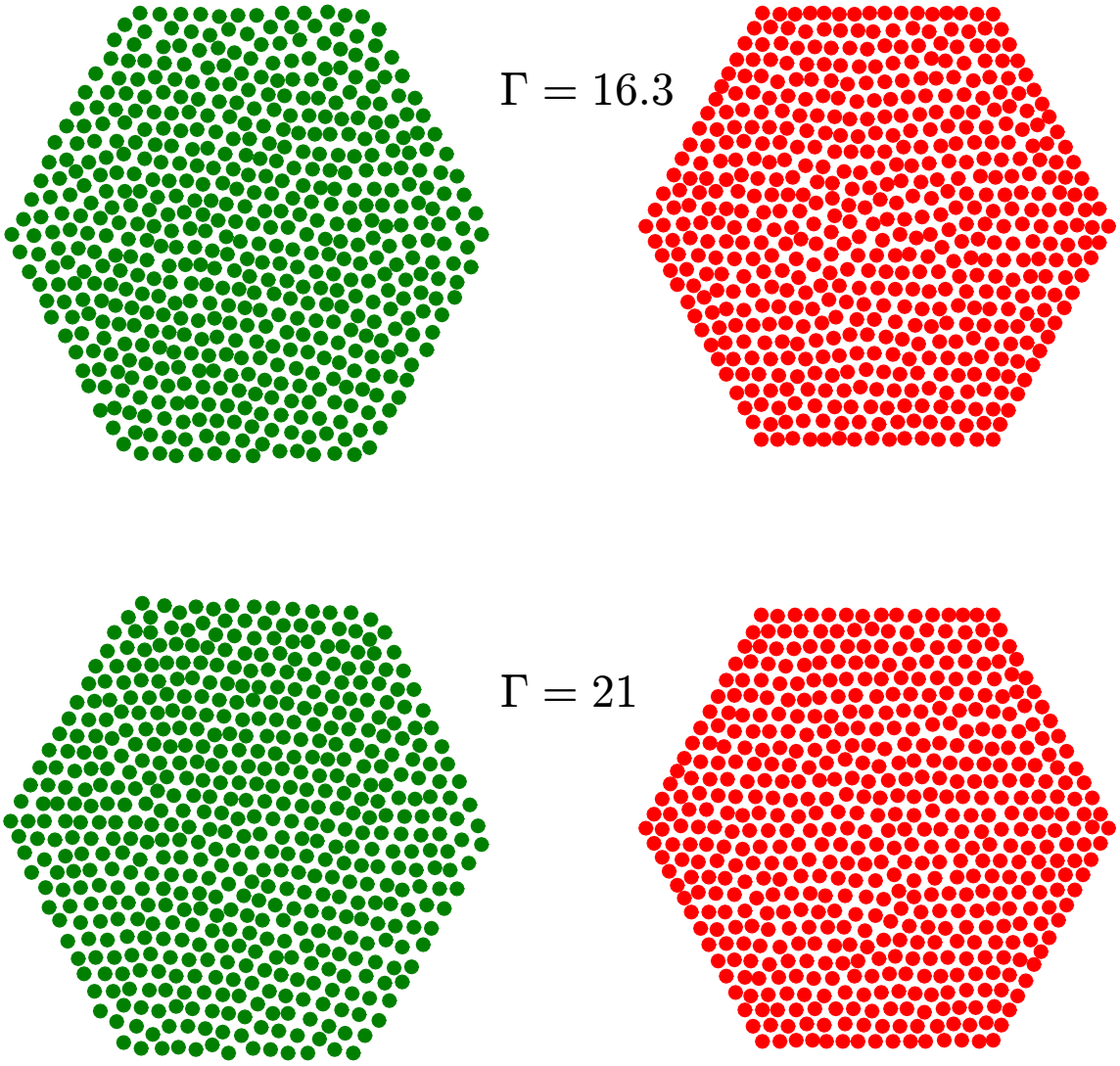

Figure 2.2 – Representative microstructures of magnetic particles for the moderate coupling regime: top snapshots corresponds to $\Gamma = 16.3$, whereas the bottom one corresponds to $\Gamma = 21$. The left panel (green) corresponds to experimental data, whereas the right one (red) corresponds to simulation data.

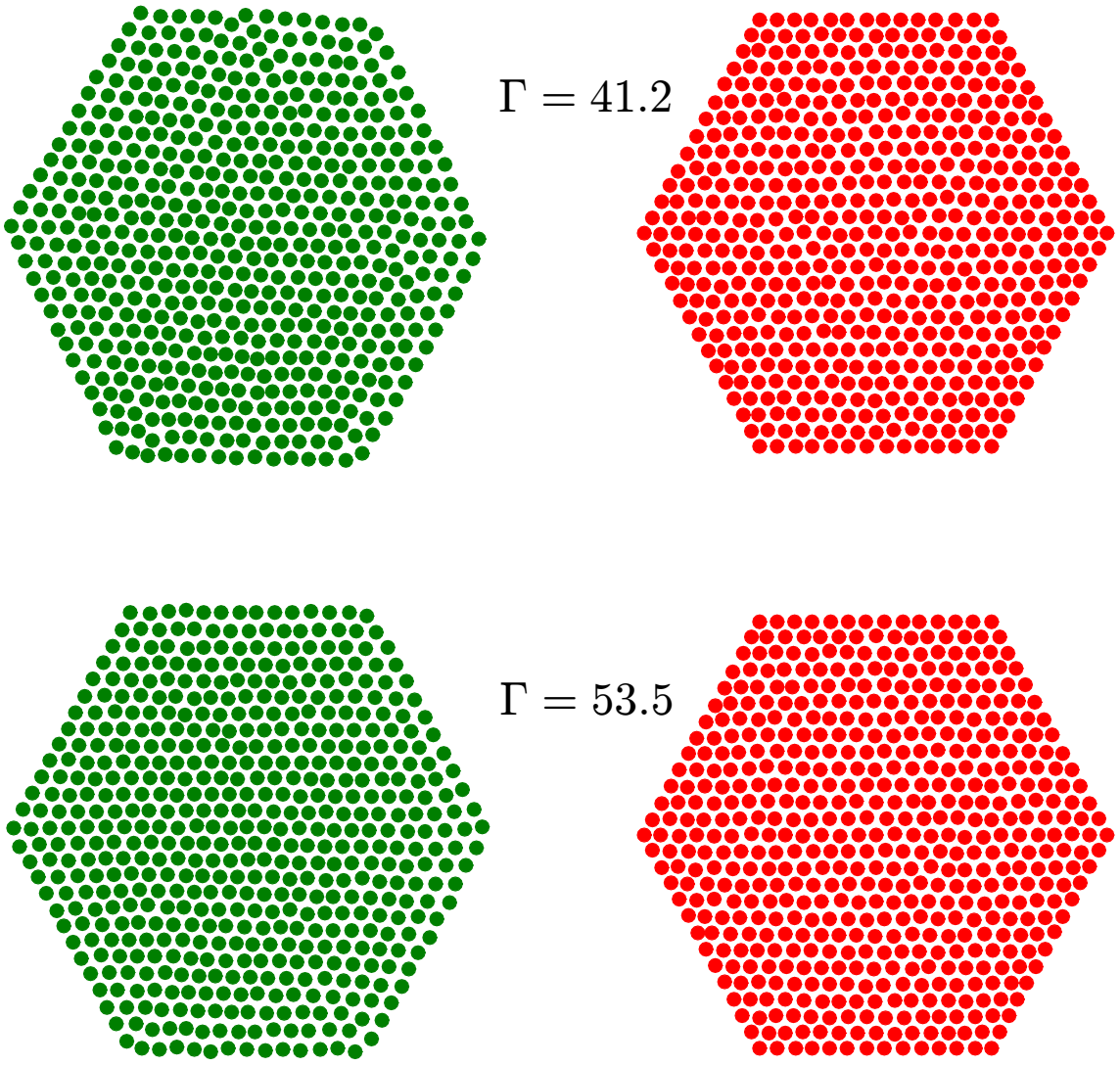

Figure 2.3 – Representative microstructures of magnetic particles for the strong coupling regime: top snapshots corresponds to $\Gamma = 41.2$, whereas the bottom one corresponds to $\Gamma = 53.52$. The left panel (green) corresponds to experimental data, whereas the right one (red) corresponds to simulation data.

2.3 Results

For the granular media, we use *millimetric* particles confined in a hexagonal box, as illustrated in Figure 2.1. In parallel, Monte Carlo simulations are performed with the same number of particles and geometry, see Methods for more details. Comparative snapshots are displayed in Fig. 2.2,2.3 for different values of the magnetic coupling parameter Γ. A visual inspection shows qualitatively identical ordering in experiments and simulations at given Γ. As expected the ordering increases with Γ and a nearly perfect triangular lattice is recovered at the highest value of $\Gamma = 53.5$. This striking agreement is going to be analysed now more quantitatively.

The first observable we consider to quantify the ordering is the pair distribution function $g(r)$ given by

$$\rho g(r) = \frac{1}{N} \left\langle \sum_{i=1}^{N} \sum_{\substack{j=1 \\ i \neq j}}^{N} \delta(r - r_{ij}) \right\rangle , \tag{2.3}$$

with ρ standing for the particle area density and $r_{ij} = |\vec{r}_i - \vec{r}_j|$ for the distance between particles i and j located at $\vec{r}_i$ and $\vec{r}_j$, respectively. This relevant quantity $g(r)$ tells us about the probability of observing two particles at distance r.

The pair distributions are plotted in Fig. 3.4 for different values of Γ. Data for colloidal systems are also provided in the moderate coupling ($\Gamma = 16.3$ and 21) regime where equilibration is sufficiently fast to avoid the pinning of the sedimented particles on the glass substrate [54], see Methods for more information. Two typical regimes are observed. The so-called hexatic phase is found at moderate dipolar coupling (here $\Gamma = 16.3$ and $\Gamma = 21$) and a solid phase emerges at high dipolar coupling (here $\Gamma = 42.2$ and $\Gamma = 53.5$). The hexatic phase is predicted by Kosterlitz-Thouless-Halperin-Nelson-Young (KTHNY) theory and is characterized by an algebraically decaying orientational correlation function $g_6(r)$ that will be discussed later. The agreement between experiments and MC simulations is remarkable and constitutes a decisive discovery bridging two well distinct scales and systems exhibiting the very same ordering. It is interesting to see that the excellent agreement between experiments on grains and simulations holds in situations where Γ is roughly doubled, going from about 20 to about 40, but also when it is varied by relatively smaller increments (roughly 20%). More specifically, in the regime of high dipolar coupling pronounced peaks in $g(r)$ set in at distances of nearest neighbors of a triangular lattice, see Fig. 3.4. At intermediate dipolar coupling the ordering still persists, but peaks get now broader and even merge. The latter feature

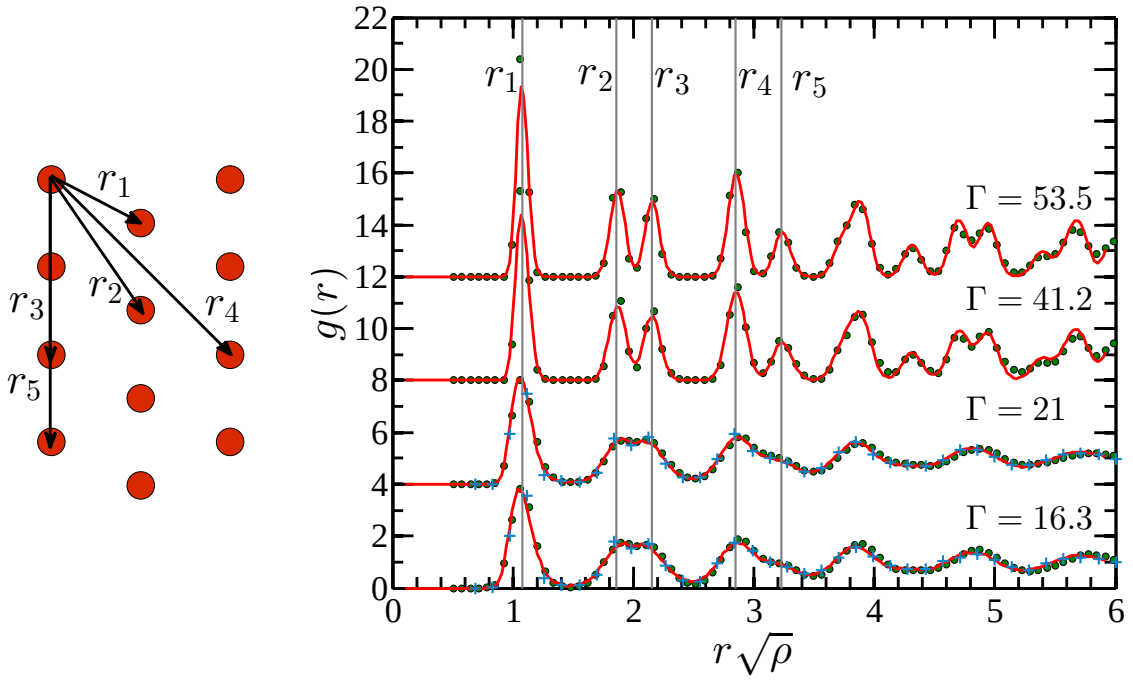

Figure 2.4 – Pair distribution functions for different values of the magnetic coupling parameter Γ. Curves are shifted upwards upon increasing Γ (16.3, 21, 42.2, and 53.5). Full lines correspond to MC simulation data, whereas dots ($\bullet$) and stars ($*$) represent granular and colloidal experimental data, respectively. Vertical lines indicate the distances between nearest neighbors for a perfect triangular lattice as illustrated in the left panel. Thereby the shortest distance between two neighbors is given by $r_1 = \left(\frac{2}{\sqrt{3}}\right)^{1/2} \frac{1}{\sqrt{\rho}} \simeq 1.075 \frac{1}{\sqrt{\rho}}$. The other distances between further neighbors appear in the following sequence: $r_2 = \sqrt{3} r_1$, $r_3 = 2r_1$, $r_4 = \sqrt{7} r_1$, $r_5 = 3r_1$, and $r_6 = 2r_2 = 2\sqrt{3} r_1$.

is especially vivid for the second and third peaks located at r_2 and r_3, respectively, see Fig. 3.4.

To further investigate the ordering of the magnetized particles, we have monitored the bond-orientational correlation function $g_6(r)$ defined as follows

$$g_6(r = |\vec{r}_m - \vec{r}_n|) = \langle \psi_6^*(\vec{r}_m) \psi_6(\vec{r}_n) \rangle \,, \tag{2.4}$$

with

$$\psi_6(\vec{r}_m) = \frac{1}{N_m} \sum_{l=1}^{N_m} e^{i6\theta_{ml}} \tag{2.5}$$

denoting the local sixfold bond orientational order parameter, where N_m is the number of nearest neighbours of particle m and θ_{ml} is the angle formed between the bond

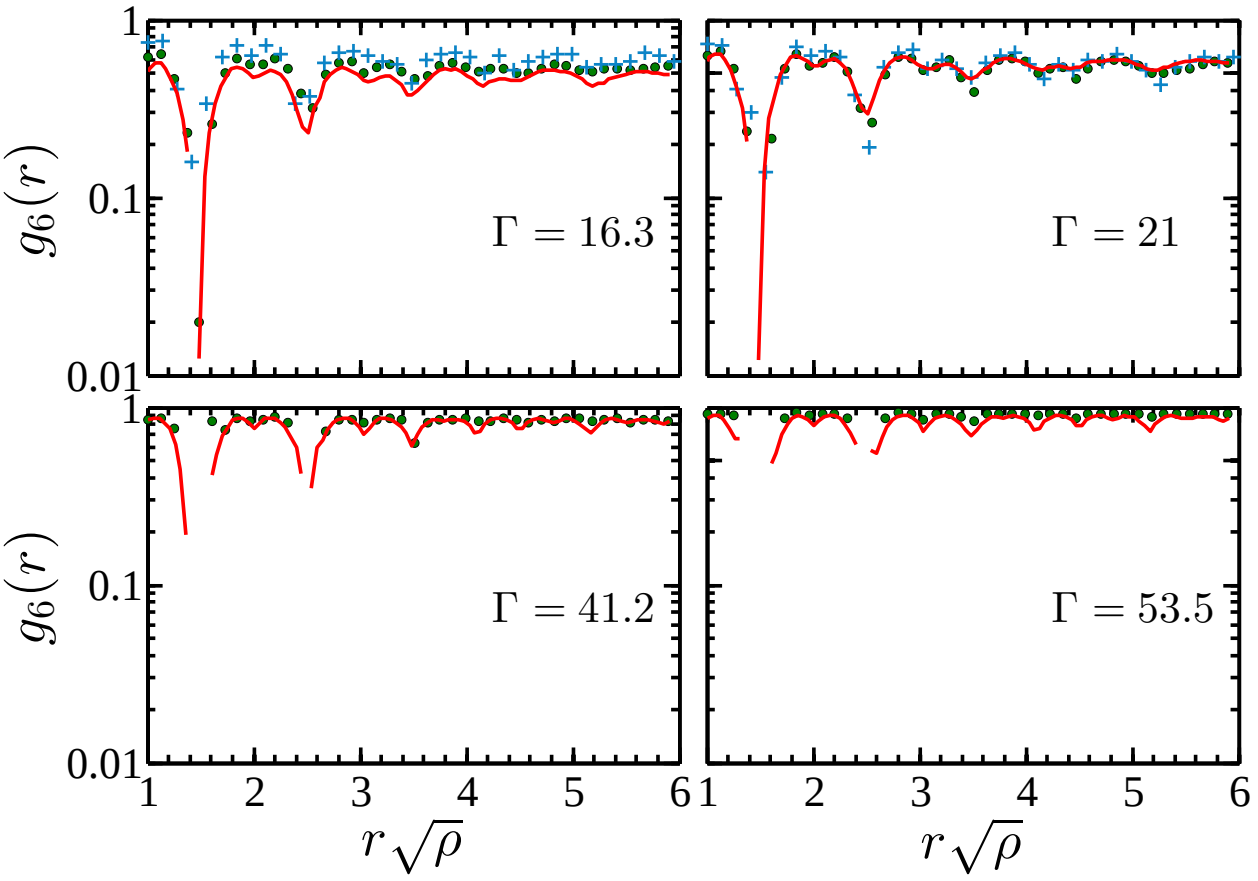

Figure 2.5 – Bond-orientational correlation functions for different values of the magnetic coupling parameter Γ.

linking particles m and l and an arbitrary prescribed reference axis.

The bond-orientational correlation functions are plotted in Fig. 2.5 for different values of Γ. At moderate coupling, good agreement between the three approaches (granular, colloidal, and simulated systems) is achieved. Upon increasing Γ, $g_6(r)$ increases and becomes close to unity at $\Gamma = 53.5$. Clearly, at high dipolar coupling (here $\Gamma = 42.2$ and $\Gamma = 53.5$) $g_6(r)$ tends to a constant in accordance with the KTHNY theory predecting (asymptotically) a constant value in the crystalline phase. For the lower values of Γ (here $\Gamma = 16.3$ and $\Gamma = 21$), it can be seen that $g_6(r)$ tend to decay algebraically. Following the KTHNY theory, this feature is a signature of the hexatic phase. Given the limited finite number of beads in the granular systems, a quantitative comparison with the KTHNY theory that holds for infinite systems is restricted.

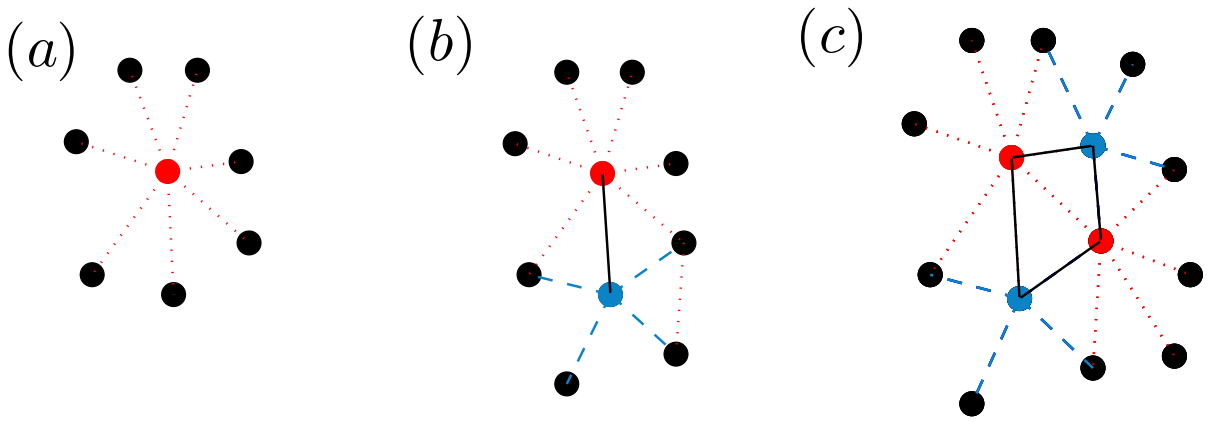

Figure 2.6 – Two dimensional hexagonal lattice defects. (a) free disclination : 7-folded lattice sites. (b) a pair of 5- and 7- fold disclination forming a free dislocation. (c) Pair of dislocations. Red particles and dotted lines symbolize a particle possesing 7 nearest neighbour, blue particles and the dashesd lines corresponds to particles having 5 nearest neighbours.

2.4 Crystalline Defects Analysis

2.4.1 Comparison of Granular and Colloidal systems

The crystallisation of two-dimensional systems is usually associated with the presence of defects especially at finite temperature. *Disclinations*, also called point defects, are one possible type of defects in a two-dimensional system. Basically disclinations correspond to a vacancy or insertion of particles in an ideal hexagonal lattice [60]. For instance instead of the normal six nearest neighbours, one could have 5-folded or 7-folded lattice sites, the latter is illustrated in figure 2.6 a. Another type of defect is *dislocation* which corresponds to adding or removing a row of particles to a perfect crystal [61]. A short dislocation (two particle row) is considered as a pair of a 5-and 7-fold defect disclinations that adjust the lattice [1] (Fig. 2.6 b). Presence of short dislocations is shown in figure 2.6 c. This configuration, also called "dislocation pair", is used to describe theoretically two-dimensional melting [23–25, 62]. The solid-hexatic transition occurs by formation of dislocation pairs, while the hexatic-liquid transition occurs by formation of pairs of disclinations [63,64]. A simple and effective way to treat the appearance of point defects in the crystal during phase transitions, is by counting the number of particles

1. Dislocation here means a pair of 5-fold and 7-fold disclinations, which is the most encountered dislocation type in the hexagonal lattice. Dislocations made up of four-fold and eight-fold disclinations are also plausible but statistically rare.

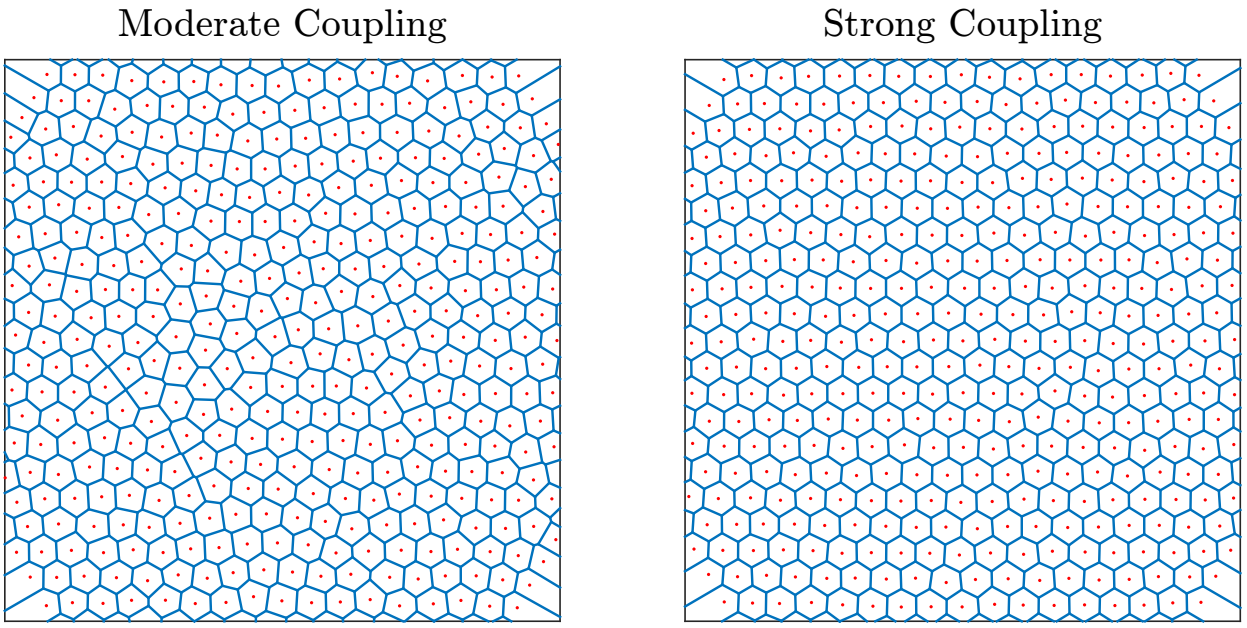

Figure 2.7 – The Voronoi diagram for two typical coupling regime: moderate coupling (Γ=21), strong coupling (Γ=53.5).

possessing a different number of neighbours than six .

This is done using the Voronoi triangulation algorithm [65, 66]. The Voronoi polygon construction can be seen as a generalisation of the Wigner-Seitz cell [67,68] but applied to disordered systems. This method allows us to assign for a given particle the number of neighbours. An illustration of the Voronoi diagram for two typical magnetic coupling regimes is shown in figure 2.7.

The distribution of the number of neighbours within the system for different magnetic coupling is deduced by counting the sides of polygon associated with each particle. It is clearly seen from figure 2.7 that for the moderate coupling there are many particles surrounded by a 7 and 5 sided polygons, which indicates rather weak ordering, while for the strong coupling the system is more ordered and mostly all particles are enclosed by 6 sided polygons (i.e 6 surrounding neighbours), indicating low presence of defects. To quantify this property the distribution of the number of neighbours is presented as a histogram in figure 2.8. When the effective temperature is high ($\Gamma = 21$), the distribution of the number of neighbours ranges between 4 and 8 neighbours. At this stage the system could be considered in the hexatic phase, since the percentages of the 5 and 7 neighbours indicate that the system is not fully ordered. Looking at these proportions in figure 2.8, interestingly we see that both systems (granular and simulations) possess almost the same percentages of defects. As the coupling strength Γ increases , we can see that the system is mainly consti-

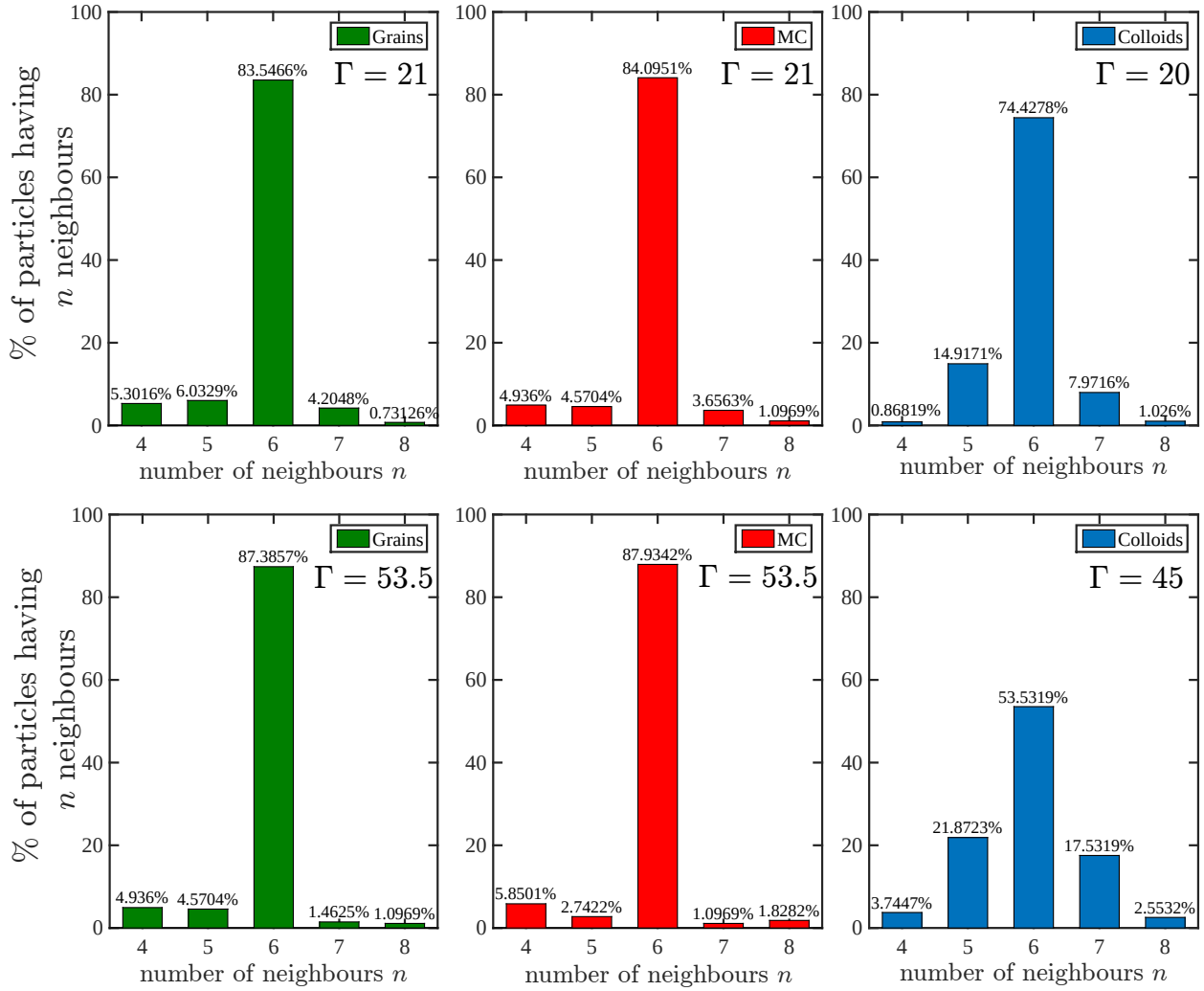

Figure 2.8 – The distribution of the number of neighbours in the system for two typical values of the coupling interaction strength Γ.

tuted of particles possessing six neighbours which indicates that it is well ordered in a perfect hexagonal lattice. However, we noticed that this agreement does not hold at high values of Γ for the colloidal experiments, and this is due to the fact that at low effective temperature the system was not well equilibrated , this part will be discussed in more details in the following section.

2.4.2 Influence of equilibration time on ordering

Our experimental setup described in the Methods chapter was a similar setup to [27–29, 52, 54]. However, in our case the two-dimensional monolayer is confined by gravity to a water/glass interface, instead of water/air interface (see [30, 69]). The general protocol used for the experiments always consist in a step wise increment

of the magnetic coupling parameter Γ.

We discuss in this section the effect of equilibration time on the number of defects present in the system. To this end, two experimental protocols were used. The first one, referred to as *fast quench* is characterized by a short waiting time for each value of Γ. The total duration of measurements for this protocol was a couple of hours. The second protocol, referred to as *slow quench* was done using the cylindrical cell covered with para-film to avoid evaporation. The slow quench protocol is characterized by longer waiting time and more intermediate values of Γ . For the slow quench protocol the highest value of Γ was reached after 17 days. The details of these two protocols and measurements are explicitly gathered in table 2.1.

Fast Quench

B (mT)	1.56	1.65	1.84	2.11	2.21	2.4	2.76
Γ	14.5	16.3	20	26.6	28.9	34	45
time(mins)	30	30	30	30	30	30	60

Slow Quench

B (mT)	0.55	0.7	0.83	1.03	1.2	1.4	1.56	1.75	1.94	2.11	2.3
Γ	1.6	2.5	3.6	5.4	7.5	10	12.8	16.3	20	23.8	28.2
time(hrs)	20	5	24	10	24	48	48	24	48	48	48

Table 2.1 – Details of the two protocols used in experiments. The time indicates the duration spent at prescribed magnetic field B corresponding to each Γ value.

Figure 2.9 shows the distribution percentages of the number of neighbours within the system at Γ=28.9 for the fast quench protocol, and at Γ=28.2 for the slow quench protocol. As it is shown in this figure the proportions of the number of particles possessing six neighbours is clearly higher in the slow quench. This leads to the conclusion that there are less defects when the time spent to reach the targeted Γ value is longer. In these colloidal experiments only the pair distribution function for the moderate coupling regime ($\Gamma = 16.3, \Gamma = 21$) were confirmed and presented in the results section. Figure 2.10 presents the distributions of the number of neighbours for each lattice site for the three systems (grains, simulation, and colloids [2]), and

2. The colloidal data in figure 2.10 were obtained with the fast quench protocol, since we couldn't reach the highest value of Γ with the slow quench due to pinning of particles on the glass substrate at long times [54].

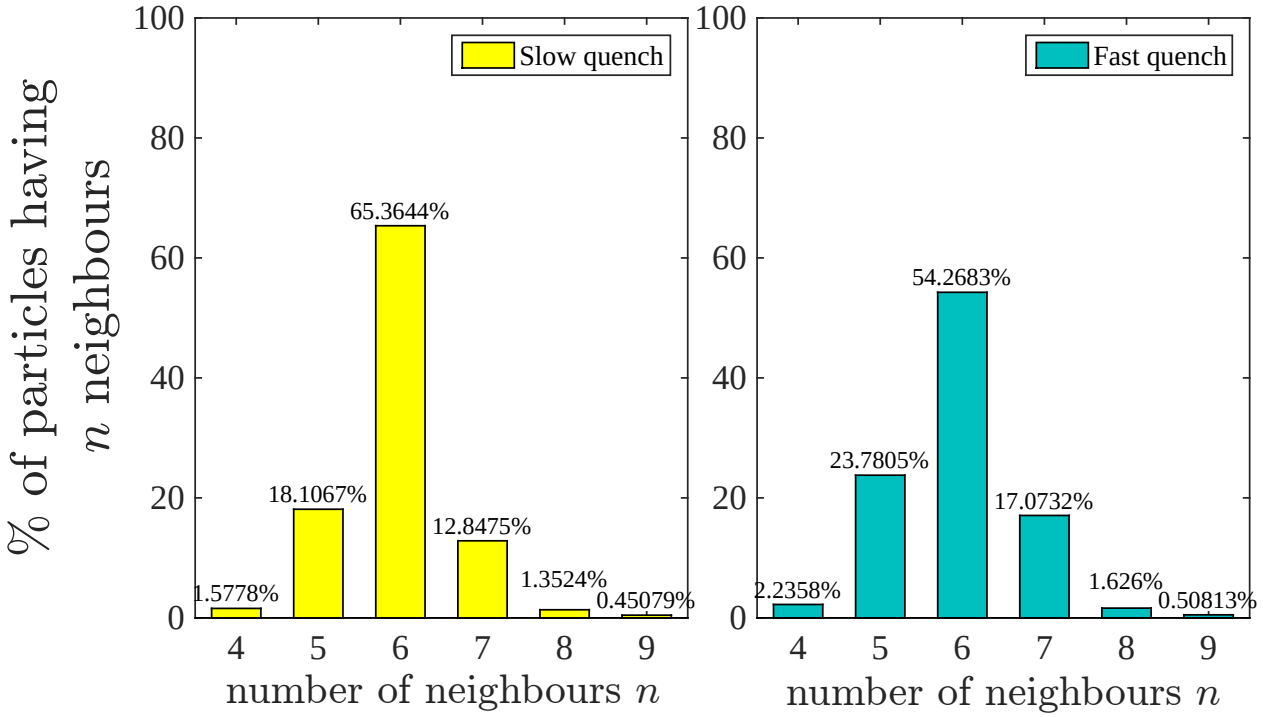

Figure 2.9 – The distribution of the number of neighbours of the two experimental protocols for coupling parameter Γ=28: The left panel corresponds to slow quench (in yellow), while the right one corresponds to fast quench (in blue).

their corresponding pair distribution function $g(r)$ for the high coupling regime [3]. The percentages in the colloidal experiment shows that the number of particles possessing six nearest neighbours is low. This indicates the presence of defects and that the system was not well equilibrated in this regime. In fact, in the colloidal experiments of other groups [27–29, 52, 54], it is always noted that when the external magnetic field $\vec{B}$ is turned on, an equilibration time of several days or weeks is necessary to equilibrate the system [70].

3. The prescribed Γ in figure 2.10 for the colloidal experiments (Γ=45) differs from the Γ value of simulations and grains (Γ=53.52), because we couldn't control a priory the particle number density ρ that is related to Γ by Eq.1.8.

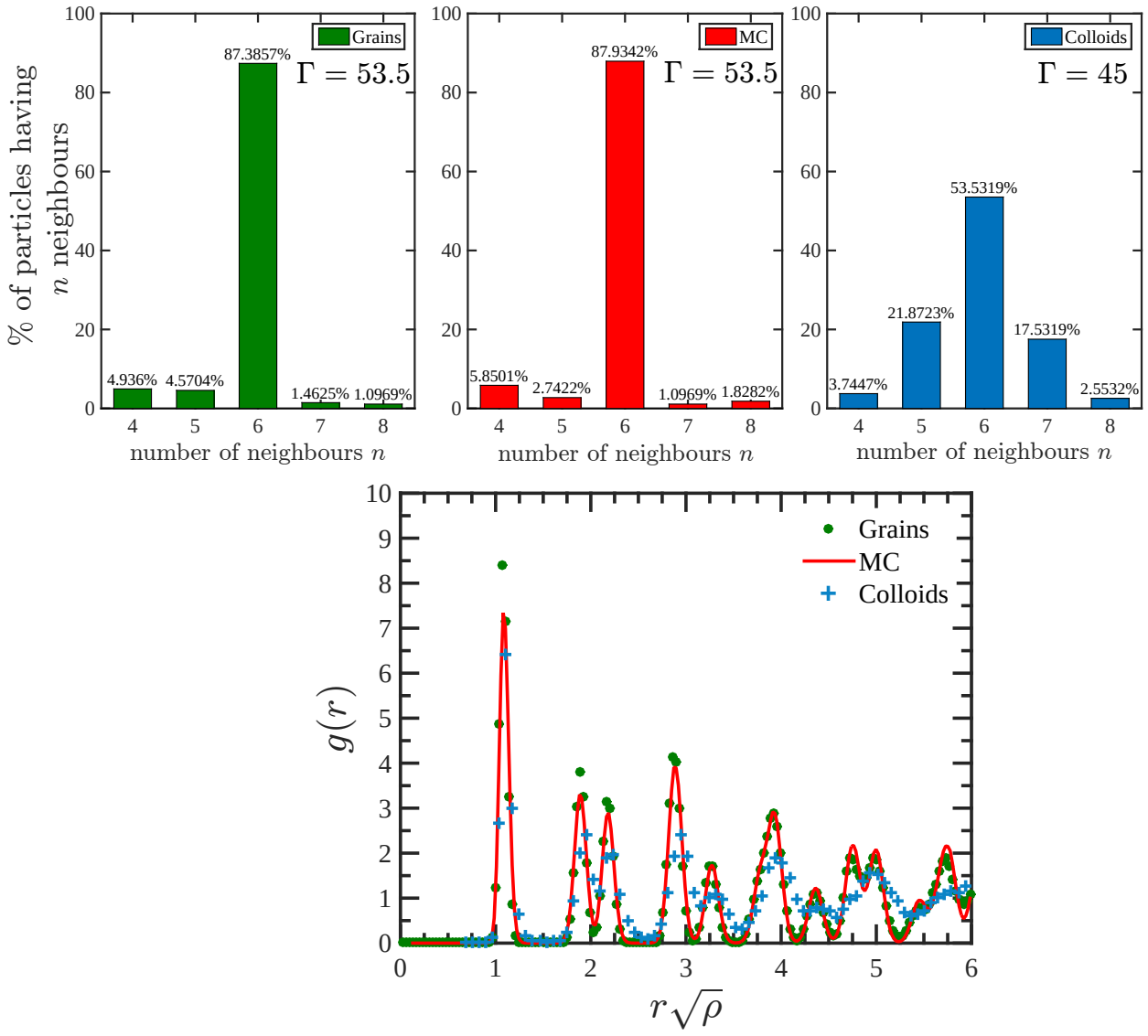

Figure 2.10 – The distribution of the number of neighbours at high magnetic coupling ($\Gamma = 53.5$ for granular experiments and MC simulations, $\Gamma = 45$ for colloidal experiments). The corresponding profiles of the pair distribution function $g(r)$ are shown in the lower panel.

2.5 Discussion

We have shown that Brownian motion can be induced in athermal systems such as granular media following a recently introduced technique [32]. In this study, the crucial energy/entropy interplay is contained in the single universal dimensionless parameter Γ. The ordering in the granular system matches quite quantitatively that found experimentally and numerically in colloidal systems. This constitutes good news for the Soft Matter community, since setting up experiments on (dry) granular

systems is much easier and convenient (e.g. considerably faster equilibration [32]) than on (wet) colloidal suspensions [30].

This being said, we are aware that our approach is only relevant for two-dimensional granular systems since gravity would cause inhomogeneity in the third dimension in contrast to colloidal systems. Besides, having to deal with repulsive and/or dilute systems allows particles to virtually not collide, and hence the effective temperature is well defined in our granular media.

This new experimental approach involving forced Brownian motion in macroscopic granular systems can be extended to study 2D binary systems [52, 53]. Quite generally speaking, a wide range of repulsive colloidal systems can be mapped onto granular ones. For the sake of the present thesis, magnetic dipolar interactions (in contrast to electrostatic forces for instance [71]) were the example of choice due to the ease of tailoring their strength. Nonetheless, partially attractive particles such as Janus spheres [72] could also be mimicked by macroscopic beads where self assembly kinetic paths could be thereby conveniently monitored. Another great advantage of fundamental importance is that reaching ground state situations (i.e. very high coupling value) is straightforward for granular media where induced noise can be merely suppressed by turning off the sources. Since both agitation and magnetic interaction could be tuned precisely and rapidly, the present granular system can be used to study the pathways of relaxation during ultrafast quenching [53].

Chapter 3

Crystallization of binary mixtures of similar dipole moments in two dimensions

3.1 Introduction

Tackling crystallization phenomena (nucleation, growth, structural defects, etc.) via colloidal crystals as analogs of conventional solids has been a very beneficial approach in condensed matter physics [4,73]. It is also well known that binary mixtures present a much richer variety of solid phases than its one-component counterpart. For instance, a one component hard-sphere system freezes into the close-packed face-centered-cubic crystal structure [74] whereas binary mixtures made up of big (denoted by A) and small (denoted by B) spheres exhibit a large basket of close-packed structures depending on their size ratio. Related superlattices of the form AB_n with $n = 1, 2, 3, 4, 5, 6, 13$ have been identified theoretically [75], in computer simulations [76], and in experiments of hard-sphere like colloids [77]. Concerning binary mixtures with *soft repulsive* interparticle interactions in three dimensions, the situation is still a puzzle that needs to be addressed.

In two dimensions, the phase behavior of binary colloidal mixtures is equally rich and intriguing. On the theoretical side, it has been studied for hard disk systems [78], and for soft repulsive pair potentials of the dipole-dipole type at zero temperature [79–81]. Computer simulations at finite temperature have been carried out for strong contrasts in dipolar moments of the constitutive particles [53, 82–84]. The relevance of the *square* AB-superlattice for *equimolar* composition theoretically predicted by Assoud et al. [79] at moderate/low reduced dipole moment was confirmed experimentally with micron-sized superparamagnetic colloidal par-

ticles [52, 53, 83] and by computer simulations [53, 83].

In this chapter, we explore the microstructures of binary mixtures with *similar* dipole moments. Typically two fundamental questions arise and will be addressed in this chapter:

— The very first question that arises is the possibilty or not of mixing at high dipolar coupling. Indeed, it is well known for a binary mixture of (small and big) hard objects that if they have a similar size, then they become unmiscible [85] (say in the high pressure limit) simply because of the impossibility of building a composite close-packed structure owing to purely excluded volume effects. For soft repulsive pair potentials the scenario is expected to be qualitatively different.

— If mixing turns out to be effective in this regime of symmetry of the dipole moments, then what are the *coexisting* phases for an equimolar composition? In this respect, it would be interesting to verify if they are in agreement with those theoretically predicted at zero temperature by Assoud et al. [79].

3.2 Model

The two particle species A and B are characterized by two dipole moments $\vec{m}_A$ and $\vec{m}_B$, respectively. The latter are assumed to be perpendicular to the confining surface mimicking the presence of a strong external electric/magnetic field. [1] The resulting pair potential is then given by:

$$U_{ij}(r) = \frac{\mu_0}{4\pi}\frac{m_i m_j}{r^3} \quad (i,j = A,B), \tag{3.1}$$

with μ_0 denoting the vacuum permeability and r the separating distance between two particles of species i and j. The constitutive particles are confined into a large hexagonal cell similar to that used in Refs. [31, 32]. The total number of particles $N_{tot} = N_A + N_B = 1027$ is fixed ($N_A = 514$ and $N_B = 513$ with N_A and N_B corresponding to the number of $A-$ and $B-$ particles, respectively) in this study so that a perfect finite triangular lattice is compatible. [2] The relative composition of the

1. This situation would experimentally correspond for instance to a binary mixture of superparamagnetic colloidal particles living at an water-air interface exposed to a strong external magnetic field yielding repulsive parallel dipole moments [52]. An analogous system in *dry granualr media* has been realized too upon mixing millimeter-sized magnetic steel and brass spheres lying on a horizontal solid substrate and subjected to a spatially uniform external magnetic field [10].

2. In order to form a defect free finite triangular lattice, the total number of particles (or sites) N_{tot} must satisfy the relation $N_{tot} = 3p^2 - 3p + 1$ where p is the number of sites per outer edge. Here $p = 19$ yields $N_{tot} = 1027$.

particles or the mixing ratio is defined as:

$$X = \frac{N_B}{N_A + N_B}. \tag{3.2}$$

Unless explicitly specified, this ratio will be fixed to 50%, i.e., (practically) the same amount of $A-$ and $B-$ particles is present in the system. All the static properties depend solely on two dimensionless parameters at prescribed composition.

1. A coupling parameter Γ defined as the ratio of the magnetic energy to the thermal energy k_BT:

$$\Gamma = \frac{\mu_0}{4\pi}\frac{m_A^2}{k_BTa^3} \tag{3.3}$$

with $a = \frac{1}{\sqrt{\rho_A}}$ representing the typical mean separation between A-particles, [3] where ρ_A stands for the surface density of the A-particles.

2. The reduced dipole moment defined as

$$m = \frac{m_B}{m_A}. \tag{3.4}$$

The total interaction potential energy of the system can now be written as

$$\beta U_{tot} = \sum_{i=1}^{N-1}\sum_{j=i+1}^{N} \beta U_{\alpha\gamma}(r_{ij}), \quad (\alpha, \beta = A, B) \tag{3.5}$$

where $\beta U_{AA} = \Gamma\frac{a^3}{r^3}$, $\beta U_{AB} = m\Gamma\frac{a^3}{r^3}$, and $\beta U_{BB} = m^2\Gamma\frac{a^3}{r^3}$.

The Hamiltonian of the system being specified, see Eq. (3.5), standard Monte Carlo simulations involving single particle moves [39, 86] have been performed for a total number of particles $N_{tot} = 1027$, with $N_A = 514$ A-particles and $N_B = 513$ B-particles. Starting with a random particle distribution, a gentle quench was applied where Γ is incremented by 10 every 10^6 steps up to the desired final value. Finite size effects are taken into account by imposing hard walls at the edges of the hexagonal cell. Typically 10^6 Monte Carlo steps are used for equilibration and statistics is gathered over additional 10^6 Monte Carlo steps.

3. On a square lattice, $a = \frac{1}{\sqrt{\rho_A}}$ would be exactly the lattice constant relative to the A-particles.

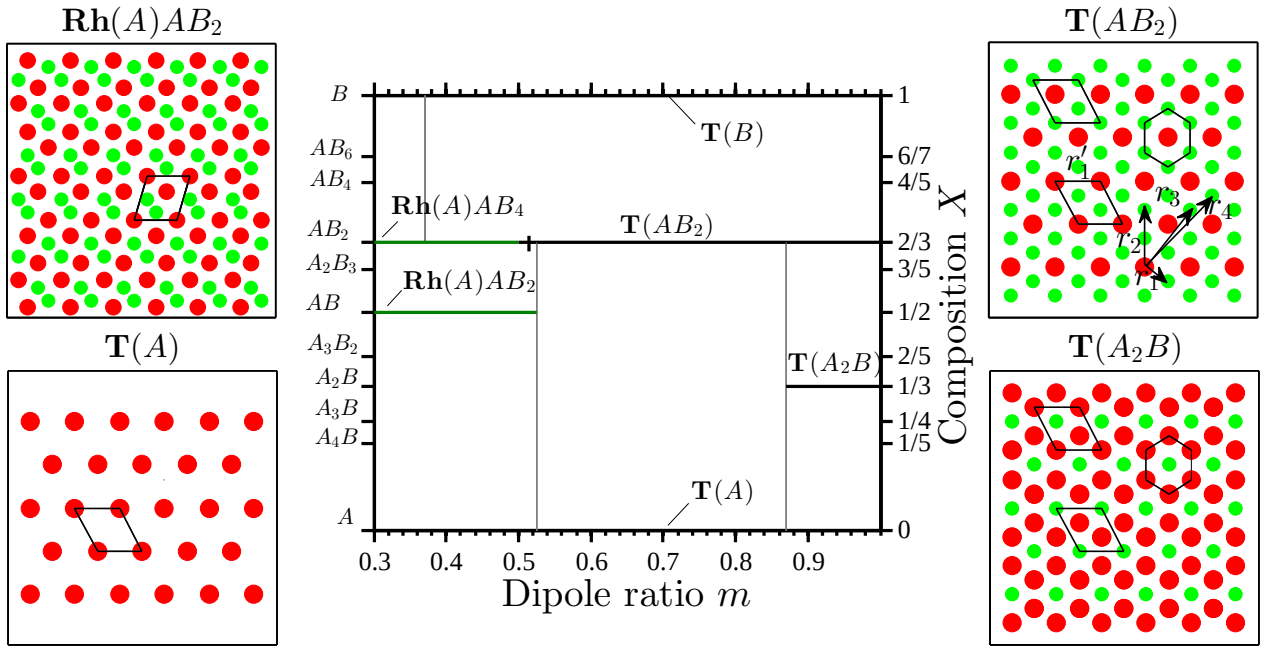

Figure 3.1 – Excerpt of the phase diagram from [79] in the (m, X) plane at *zero temperature* predicted theoretically. [79] The same notation as in Ref. [79] is used here. The relevant phases for the current study are illustrated. The relative positions of the four nearest AB neighbours for the triangular structure $\mathbf{T}(AB_2)$ [or equivalently $\mathbf{T}(A_2B)$ for symmetry reasons] are sketched: $r_1/a = \left(\frac{1}{\sqrt{3}}\right)^{1/2} \simeq 0.76$, $r_2 = 2r_1$, $r_3 = \sqrt{7}r_1$, and $r_4 = \sqrt{13}r_1$.

3.3 Results

We first briefly recall the main features of the phase diagram in the (m, X)-plane predicted theoretically at zero temperature by Assoud et al. [79], see Fig. 3.1.[4] Thereby, a large dipole strength asymmetry corresponds to low values of the reduced dipole moment m ($m \lesssim 0.5$), whereas a weak asymmetry corresponds to high values of m ($m \gtrsim 0.5$). At moderate dipolar parameter $0.3 \lesssim m \lesssim 0.5$, a stable equimolar compound is found with a rhombic unit cell, $\mathbf{Rh}(A)AB_2$, see Fig. 3.1. For larger values of m, phase coexistences are predicted, see Fig. 3.1. It is seen that the phase $\mathbf{T}(AB_2)$ plays a crucial role and should always be present for equimolar composition ($X = 1/2$) as a coexisting phase, see Fig. 3.1. The other accompanying phase is either (i) the pure A triangular phase $\mathbf{T}(A)$ for $0.5 \lesssim m \lesssim$

4. This is a slightly simplified version of the original phase diagram [79], see Fig. 3.1, where some phases are absent in the regime of low dipolar paramaters $m \lesssim 0.3$ and high B-particles concentration ($X > 0.8$). In the scope of our present study, aiming equimolar composition (i.e., $X = 0.5$) and essentially weak polar asymmetry (i.e., $m \gtrsim 0.5$), these missing phases are not relevant.

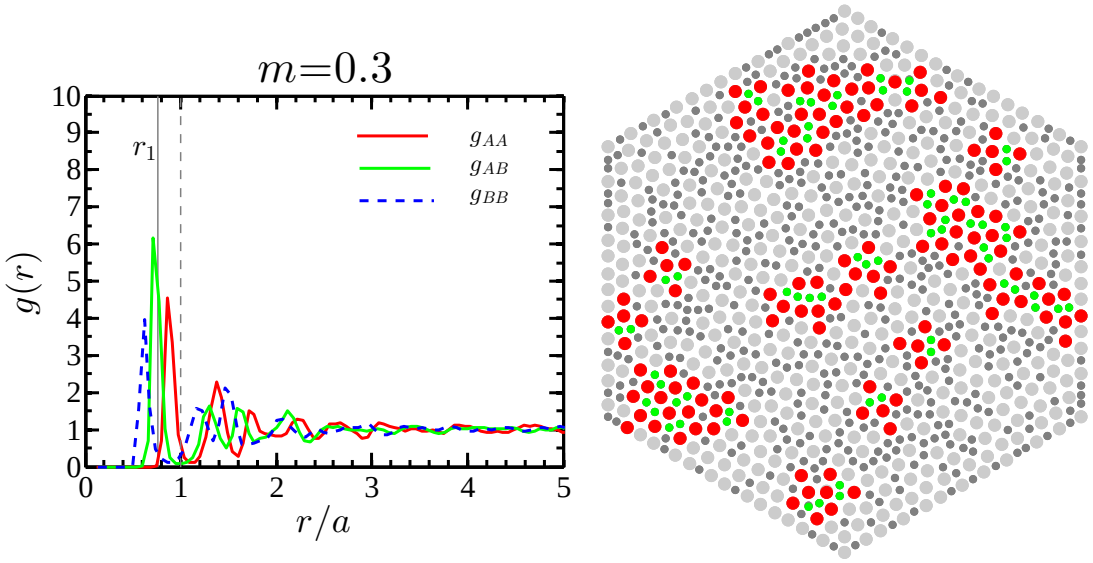

Figure 3.2 – Partial pair distribution functions at reduced dipole moment $m = 0.3$ at equimolar composition $X = 0.5$ and dipolar interaction coupling $\Gamma = 100$. The distances r_1 (already defined in Fig. 3.1) and $r_\square = a$ are emphasized with vertical lines. They represent nearest AB neighbors (solid line) in the triangular phase $\mathbf{T}(A_2B)$ and nearest AA neighbors (dashed line) in the square phase $S(AB)$, respectively. A typical perfect unit cell of $\mathbf{Rh}(A)AB_2$ is depicted in Fig. 3.1. An illustrative simulation snapshot is also provided revealing $\mathbf{Rh}(A)AB_2$-like patches. Large A-particles are shown in red if they belong to a $\mathbf{Rh}(A)AB_2$ environment, whereas small B-particles appear in green in such a case. Otherwise big and small particles appear in light grey/dark grey, respectively.

0.9 or (ii) the composite phase $\mathbf{T}(A_2B)$ at weak dipolar asymmetry (i.e., $m \gtrsim 0.9$). It is precisely these striking features that we would like to investigate by computer simulations. Two important questions arise:

1. Do composite phases of similarly magnetized/polarized particles show up at finite temperatures representative of experimental conditions?
2. If yes, do they correspond to the phases predicted by Assoud et al. [79], see Fig. 3.1?

We shall present our results for several values of the dipole strength asymmetry ($m \geq 0.3$). The interaction coupling strength Γ is fixed, unless explicitly differently stated, to $\Gamma = 100$. The choice of this value for Γ is motivated by previous experimental studies where very similar values were employed [53, 83] A detailed microstrucural study is carried out with the help of (i) partial pair distribution functions: $g_{AA}(r)$, $g_{BB}(r)$ and $g_{AB}(r)$, and (ii) instructive snapshots.

Before answering the two intriguing questions advocated just above, we are going to discuss the regime of moderate reduced dipole parameter, namely $m = 0.3$

in this work. Interestingly, rhombic like crystallites of the $\mathbf{Rh}(A)AB_2$-type are well present and dominant in the system at finite temperature, see Fig. 3.2. This feature qualitatively confirms the theoretical prediction, compare Fig. 3.1 with Fig. 3.2. To be more quantitative, we are going to analyze the corresponding partial pair distribution functions that can also be found on Fig. 3.2. It is clearly seen that the first neighbour peak of the triangular and square phases are absent. More precisely:

— The location of the first peak in g_{AA} occurs at $r/a \simeq 0.86$ clearly smaller than unity, see Fig. 3.2. Therefore, the square phase $\mathbf{S}(AB)$ (not shown in Fig. 3.1 but easily identifiable around $m = 0.1$ in Ref. [79]) characterized by a first peak in g_{AA} at $r_\square/a := 1$ does not show up. Similarly, the triangular phase $\mathbf{T}(A)$ characterized by a first peak in g_{AA} at $r_1/a := \left(\frac{1}{\sqrt{3}}\right)^{1/2} \simeq 0.76$ is marginally apparent. [5]

— The occurrence of triangular phases of the type $\mathbf{T}(AB_2)$ or $\mathbf{T}(A_2B)$ should be accompanied by a first peak in g_{AB} at r_1, see Fig. 3.1. This is not verified here, see Fig. 3.2, where the first peak in g_{AB} is at $r/a \simeq 0.71$.

We now turn to the main finding of our simulation data that concern the regime of similarly magnetized/polarized dipoles (i.e., $m \gtrsim 0.5$). An overview of our results can be found in Fig. 3.3. In good qualitative agreement with the theoretical prediction at zero temperature, compare Fig. 3.3 with Fig. 3.1, the phase $\mathbf{T}(AB_2)$ is well present in the microstructure at all m values. As a matter of fact, a finite temperature allows the appearance of all the predicted relevant triangular phases [i.e., $\mathbf{T}(A)$, $\mathbf{T}(B)$ and especially $\mathbf{T}(AB_2)$ and $\mathbf{T}(AB_2)$], see Fig. 3.3, in a proportion that reflects the zero temperature phase diagram, compare Fig. 3.1 with Fig. 3.3. Two relevant effects supporting the theoretically predicted phase behavior at zero temperature (compare Fig. 3.3 with Fig. 3.1) can be pointed out:

1. The global surface fraction of $\mathbf{T}(AB_2)$ and $\mathbf{T}(A_2B)$ patches tends to increase with growing similarity in dipole moments (i.e., m).
2. The ratio of surface fraction of $\mathbf{T}(A_2B)$ phase and that of $\mathbf{T}(AB_2)$ one is increasing with m. At high dipolar similarity, especially at $m = 0.9$ (see Fig. 3.3), the phase $\mathbf{T}(A_2B)$ occupation becomes quite comparable to that of phase $\mathbf{T}(AB_2)$.

To further deepen our understanding of the phase behavior of this binary mixture we are going to investigate the related partial pair distribution functions. The latter

5. One has to bear in mind that we always have a binary mixture at equimolar composition $X = 0.5$. Thereby, in case of phase separation involving a phase $\mathbf{T}(A)$, the *local* surface density would become (at most) $2\rho_A$ for the A-particles. Note that r_1 corresponds also to the lattice constant of the triangular lattice of surface (site) density $\rho_A + \rho_B = 2\rho_A$.

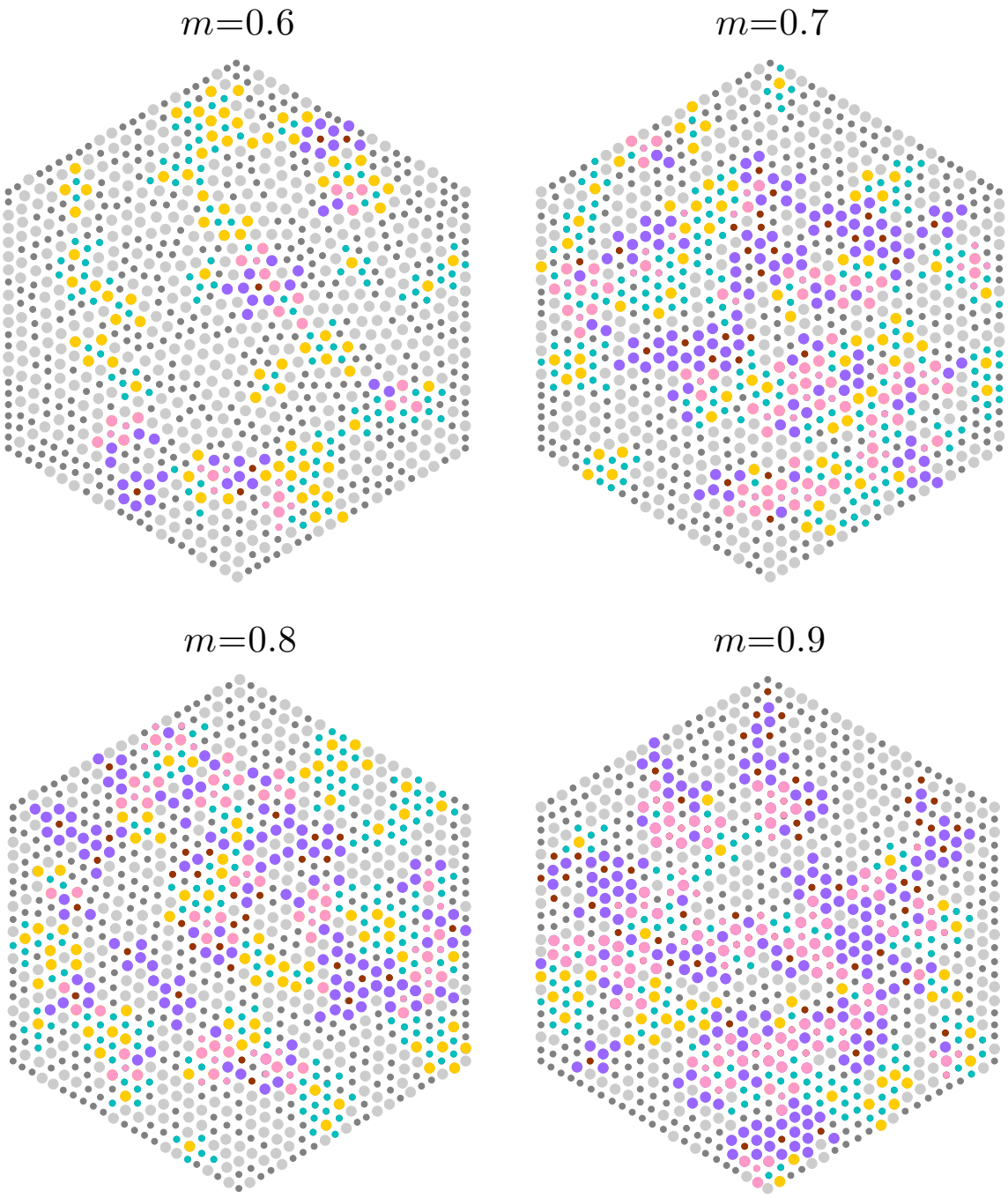

Figure 3.3 – Simulation snapshots for four values of the reduced dipole moment $m = 0.6, 0.7, 0.8$, and 0.9 at equimolar composition $X = 0.5$ and dipolar interaction coupling $\Gamma = 100$. Big A-particles are shown in yellow if they belong to a $\mathbf{T}(AB_2)$ environment (see Fig. 3.1 for typical unit cells), in purple if they belong to a $\mathbf{T}(A_2B)$ one, in pink if they belong to both, and light grey otherwise. Small B-particles are depicted in light blue if they belong to a $\mathbf{T}(AB_2)$ environment (see Fig. 3.1 for typical unit cells), in brown if they belong to $\mathbf{T}(A_2B)$, in pink (same color as for A-particles) if common to both, and dark grey otherwise.

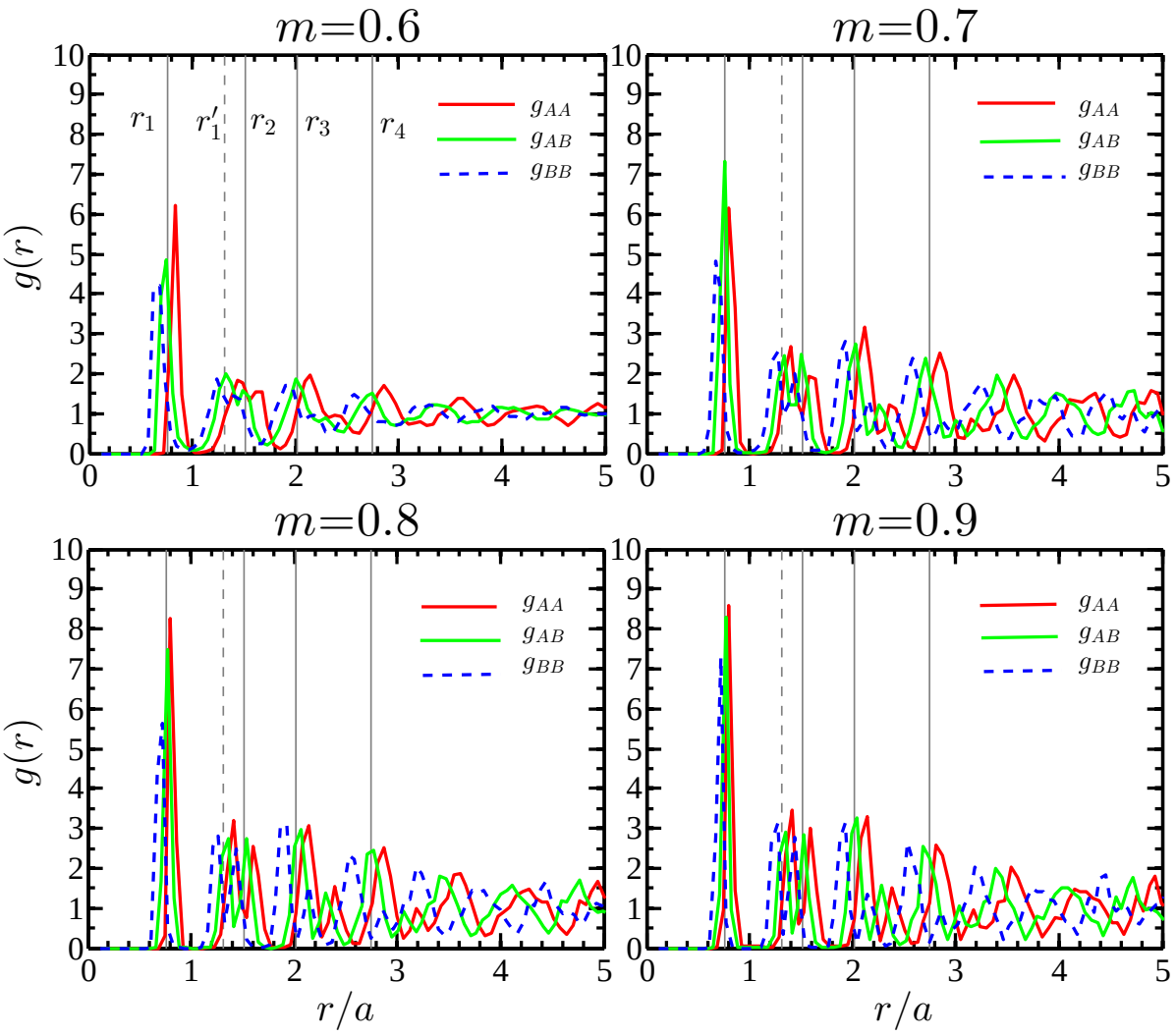

Figure 3.4 – Partial pair distribution functions for four values of the reduced dipole moment $m = 0.6, 0.7, 0.8,$ and 0.9 at equimolar composition $X = 0.5$ and dipolar interaction coupling $\Gamma = 100$. The corresponding simulation snapshots can be found in Fig. 3.3. The four vertical solid lines represent the four nearest AB neighbor distances (r_1, r_2, r_3, r_4) depicted in Fig. 3.1 in the $\mathbf{T}(AB_2)$/$\mathbf{T}(A_2B)$-phase. The vertical dashed line indicates the nearest AA/BB distance in the $\mathbf{T}(AB_2)$/$\mathbf{T}(A_2B)$-phase corresponding to $r_1' = \sqrt{3}r_1$, see also Fig. 3.1. The distance $r_\triangle$ is not shown for the sake of clarity.

are displayed in Fig. 3.4 for the same parameters of the previously discussed snapshots in Fig. 3.3. A striking feature in these profiles of $g_{AA}(r)$, $g_{AB}(r)$, and $g_{BB}(r)$, is a *common high first peak* around r_1, see Fig. 3.4. This remarkable property of *mixing* has the following origins:

— The first high peak in g_{AB} precisely located at r_1, see Fig. 3.4, is the signature of the $\mathbf{T}(AB_2)$ and $\mathbf{T}(A_2B)$ phases, see also Fig. 3.3. AB correlations mediated by *alloy patches*, see grayed particles in Fig. 3.3, should also contribute

to some extent to this peak in g_{AB}.

— On the other hand, the first peak in g_{BB} and g_{AA} located in the vicinity of r_1, see Fig. 3.4, stems from the shortest BB- and AA-separation in the $\mathbf{T}(AB_2)$ and $\mathbf{T}(A_2B)$ phases (see also Fig. 3.1), respectively.[6] A closer visual inspection of the microstructures of Fig. 3.3 reveals that patches (grayed particles) of the phase $\mathbf{T}(A)$ and $\mathbf{T}(B)$ should also to some extend contribute to the peaks around r_1 in g_{AA} and g_{BB}, respectively.

The crystallization into composite triangular phases [i.e., $\mathbf{T}(AB_2)$ and $\mathbf{T}(A_2B)$] is now addressed in more detail. As far as g_{AB} is concerned, it unambiguously exhibits the four peaks attributed to the pronounced correlations between AB particles at the four nearest AB-distances in a $\mathbf{T}(AB_2)$/$\mathbf{T}(A_2B)$-phase, see Fig. 3.4. The height of the first peak in g_{AB} at r_1 increases with m, in agreement with the microstructural analysis, where a m-enhanced crystallization into $\mathbf{T}(AB_2)$ and $\mathbf{T}(A_2B)$ patches is found, compare Fig. 3.3 with Fig. 3.4. Similarly, the height of the first peak in g_{AA} and g_{BB} around r_1 increases with m, see Fig. 3.4. The first neighbor distance between minority species (i.e., AA and BB distances in $\mathbf{T}(AB_2)$ and $\mathbf{T}(A_2B)$, respectively) designated by $r_1' := \sqrt{3}r_1$, see Fig. 3.1, is expected to be the location of peaks in g_{AA} and g_{BB}. This feature is indeed well confirmed, see Fig. 3.4, and is especially relevant at high dipolar similarity (e.g., $m = 0.8, 0.9$) where patches of $\mathbf{T}(AB_2)$ and $\mathbf{T}(A_2B)$ are dominant, see Fig. 3.3.

3.4 Concluding remarks

In conclusion, the crystallization of binary mixtures of dipolar particles at high dipolar coupling has been investigated by computer simulations for an equimolar composition. The relevant features of the phase diagram at zero temperature predicted theoretically by Assoud et al. [79] are well reproduced. As a major result, a strong mixing involving triangular phases $\mathbf{T}(AB_2)$ and $\mathbf{T}(A_2B)$ is found for similarly magnetized/polarized particles. At moderate reduced dipole moment m, the rhombic phase $\mathbf{Rh}(A)AB_2$ emerges *excluding* traces of the square phase $\mathbf{S}(AB)$ (stable at low m) and the triangular composite ones $\mathbf{T}(AB_2)$ and $\mathbf{T}(A_2B)$ (stable at higher m).

We finish with the experimental possibility of realizing such dipolar mixtures with low dipolar asymmetry. Recently, it was shown, at the level of one-component

6. A careful inspection of the peaks around r_1 reveals that their position (say r_{AA} for g_{AA}, r_{AB} for g_{AB}, and r_{BB} for g_{BB}) always obeys $r_{BB} < r_{AB} < r_{AA}$, see Fig. 3.4. This feature merely reflects the growing repulsion when going from a BB-pair to a AA-pair via a AB-pair.

systems, that excited granular media [31] could be of great help to quantitatively mimic crystallization of colloidal particles. A similar approach could be advantageously used to study binary mixtures. This would be especially relevant in this regime of high dipolar similarity ($0.5 \lesssim m < 1$), where a colloidal suspension with weakly contrasted bidispersity in size is awkward to achieve.

Conclusion and Perspectives

We have studied the crystallization of two-dimensional systems made up of repulsive dipolar particles. Performing experiments as well as computer simulations on *colloidal systems*, microstructural properties are analyzed via order parameters such as the pair distribution function or the orientational correlation function. The first part of the manuscript treats about one-component systems, whereas the second part deals with two-component systems.

Concerning the one-component case, we have shown that Brownian motion can be induced in athermal systems such as granular media following a technique developed in the GRASP Laboratory in Liége [32]. In both granualar and colloidal systems the constitutive particles lie on a substrate and are paramagnetic. Thereby, the repulsive interparticle interaction can be precisely controlled by varying the magnitude of an external magnetic field $\vec{B}$ normal to the surface [31]. The granular particles are subjected to horizontal mechanical vibration that can be seen as the analog of thermal agitation. Therefore, the magnetic interaction for both systems competes with thermal agitation and the ratio of the magnetic to thermal energy is then characterized by an inverse reduced temperature: the dimensionless magnetic coupling parameter Γ. Excellent agreement between (i) experimental data on granular systems and (ii) experimental as well as simulation data on colloidal systems throughout the range of the magnetic coupling parameter Γ is found for the pair distribution as well as the orientational correlation functions. Excellent agreement concerning these two order parameters was found, for moderate and high magnetic coupling regimes. These results reveal that well characterized granular systems could function as 'wet models' for studying the case of phase transitions in two dimensional systems. This fundamental finding constitutes good news for the Soft Matter community, since experiments on *dry* granular systems circumvent usual drawbacks encountered in *wet* colloidal suspensions especially the long equilibration time.

The second part of this thesis addresses the two-component case. Binary mixtures made up of particles with similar dipole moments are investigated by computer

simulations. Using Monte Carlo methods, a quantitative structural study based on partial pair distribution functions and microstructure snapshots is presented for high dipolar coupling Γ. At equimolar composition, the relevance of the coexistence of triangular superlattices with stoichiometry AB_2 and A_2B is revealed, with $A(B)$ standing for the large(small) dipole moments. This finding is in excellent qualitative agreement with the zero temperature theoretical predictions [79]. More specifically, these found superlattices are relevant for a quite large range in the regime of similar dipole moments m_A and m_B ($0.6 \lesssim m_B/m_A \leq 1$).

The related findings of this research work can serve as starting points for new exciting future projects. Granular media could be further exploited to understand ordering due to the crucial balance of energy vs entropy. A promising situation concerns a tilted external magnetic field that allows exploring repulsive as well as *attractive* interparticle interactions depending on the relative angle with the substrate. In this scenario, despite of some existing preliminary theoretical results in the literature [81,87], the case of binary mixtures is poorly understood at tilted field. Hence, experiments involving both colloidal and granular systems corroborated by simulations, would be of great help to elucidate the ordering at tilted field.

List of Figures

Bibliography

[1] Thomas Graham. Liquid diffusion applied to analysis. *Philosophical transactions of the Royal Society of London*, pages 183–224, 1861. 3

[2] R Brown. Abrief account of microscopical observations made in the months of june, july and august 1827, on the particles contained in the pollen of plants, and on the general existence of active molecules in organic and inorganic bodies. *Edin. Phil. J*, 5:358, 1828. 3

[3] Hartmut Löwen. Melting, freezing and colloidal suspensions. *Physics Reports*, 237(5):249–324, 1994. 4

[4] U Gasser. Crystallization in three- and two-dimensional colloidal suspensions. *J. Phys.: Condens. Matter*, 21(20):203101, 2009. 4, 45

[5] H Löwen, EC Oguz, L Assoud, and R Messina. Colloidal crystallization between two and three dimensions. *Advances in Chemical Physics*, 148:225, 2012. 4

[6] K. Binder. *J. Non-Equilib. Thermodyn.*, 23:1, 1998. 4

[7] Pawel Pieranski. Colloidal crystals. *Contemporary Physics*, 24(1):25–73, 1983. 4

[8] Costas M Soukoulis. *Photonic crystals and light localization in the 21st century*, volume 563. Springer Science & Business Media, 2012. 4

[9] Sang Hyun Park and Younan Xia. Assembly of mesoscale particles over large areas and its application in fabricating tunable optical filters. *Langmuir*, 15(1):266–273, 1999. 4

[10] Michael B. Hay, Richard K. Workman, and Srinivas Manne. Two-dimensional condensed phases from particles with tunable interactions. *Phys. Rev. E*, 67(1), Jan 2003. 5, 46, 57

[11] Dayang Wang and Helmuth Möhwald. Template-directed colloidal self-assembly–the route to 'top-down'nanochemical engineering. *Journal of Materials Chemistry*, 14(4):459–468, 2004. 5, 57

[12] Mitsutaka Haruta and Hiroki Kurata. Direct observation of crystal defects in an organic molecular crystals of copper hexachlorophthalocyanine by stem-eels. *Scientific reports*, 2, 2012. 5, 57

[13] RE Peierls. Remarks on transition temperatures. *Helv. Phys. Acta*, 7(2):81–83, 1934. 4

[14] N. D. Mermin. Crystalline order in two dimensions. *Phys. Rev.*, 176:250–254, Dec 1968. 4

[15] Piotr Pierański, Jerzy Małecki, Wojciech Kuczyński, and Krzysztof Wojciechowski. A hard-disc system, an experimental model. *Philos. Mag. A*, 37(1):107–115, 1978. 4

[16] Pawel Pieranski. Two-dimensional interfacial colloidal crystals. *Phys. Rev. Lett.*, 45:569–572, Aug 1980. 4

[17] C. A. Murray and D. H. Van Winkle. Experimental observation of two-stage melting in a classical two-dimensional screened coulomb system. *Phys. Rev. Lett.*, 58:1200–1203, Mar 1987. 4

[18] A. T. Skjeltorp. One- and two-dimensional crystallization of magnetic holes. *Phys. Rev. Lett.*, 51:2306–2309, Dec 1983. 4

[19] B. J. Alder and T. E. Wainwright. Phase transition in elastic disks. *Phys. Rev.*, 127:359–361, Jul 1962. 4

[20] Søren Toxvaerd. Phase transitions in a two-dimensional system. *Phys. Rev. Lett.*, 44:1002–1004, Apr 1980. 4

[21] D. Frenkel and J. P. McTague. Evidence for an orientationally ordered two-dimensional fluid phase from molecular-dynamics calculations. *Phys. Rev. Lett.*, 42:1632–1635, Jun 1979. 4

[22] R. C. Gann, Sudip Chakravarty, and G. V. Chester. Monte carlo simulation of the classical two-dimensional one-component plasma. *Phys. Rev. B*, 20:326–344, Jul 1979. 4

[23] John Michael Kosterlitz and David James Thouless. Ordering, metastability and phase transitions in two-dimensional systems. *Journal of Physics C: Solid State Physics*, 6(7):1181, 1973. 4, 38

[24] David R Nelson and BI Halperin. Dislocation-mediated melting in two dimensions. *Phys. Rev. B*, 19(5):2457, 1979. 4, 38

[25] A. P. Young. Melting and the vector coulomb gas in two dimensions. *Phys. Rev. B*, 19:1855–1866, Feb 1979. 4, 38

[26] Klaus Zahn. *Liquides et cristaux colloidaux magnetiques a deux dimensions:structures,dynamique et transition de phase*. PhD thesis, Université de Strasbourg, 1997. 4, 9

[27] K. Zahn, J. M. Méndez-Alcaraz, and G. Maret. Hydrodynamic interactions may enhance the self-diffusion of colloidal particles. *Phys. Rev. Lett.*, 79:175–178, Jul 1997. 4, 9, 29, 32, 40, 42

[28] K. Zahn, R. Lenke, and G. Maret. Two-stage melting of paramagnetic colloidal crystals in two dimensions. *Phys. Rev. Lett.*, 82:2721–2724, Mar 1999. 4, 29, 40, 42

[29] K. Zahn and G. Maret. Dynamic criteria for melting in two dimensions. *Phys. Rev. Lett.*, 85:3656–3659, Oct 2000. 4, 40, 42

[30] Florian Ebert, Patrick Dillmann, Georg Maret, and Peter Keim. The experimental realization of a two-dimensional colloidal model system. *Rev. Sci. Instrum.*, 80:083902, 2009. 6, 40, 44, 57

[31] René Messina, Sarah Aljawhari, Lydiane Bécu, Julien Schockmel, Geoffroy Lumay, and Nicolas Vandewalle. Quantitatively mimicking wet colloidal suspensions with dry granular media. *Sci. Rep.*, 5:10348, 06 2015. 4, 46, 54, 55

[32] J. Schockmel, E. Mersch, N. Vandewalle, and G. Lumay. Melting of a confined monolayer of magnetized beads. *Phys. Rev. E*, 87(6):062201, JUN 10 2013. 5, 16, 29, 30, 31, 43, 44, 46, 55, 59

[33] Dynabeads® epoxy m450 invitrogen 5 ml from life technologies.com. 7

[34] M. Benelmekki, Ll. M. Martinez, J. S. Andreu, J. Camacho, and J. Faraudo. Magnetophoresis of colloidal particles in a dispersion of superparamagnetic nanoparticles: theory and experiments. *Soft Matter*, 8:6039–6047, 2012. 9

[35] W. C. Elmore. The magnetization of ferromagnetic colloids. *Phys. Rev.*, 54:1092–1095, Dec 1938. 9

[36] J Frenkel and J Dorfman. Spontaneous and induced magnetisation in ferromagnetic bodies. *Nature*, 126(3173):274–275, 1930. 9

[37] Eric W Weisstein. Hex number. 2003. 16

[38] Group for research and applications in statistical physics. 16, 17, 29, 58

[39] M. P. Allen and D. J. Tildesley. *Computer Simulations of Liquids*. Clarendon Press, Oxford, 1987. 16, 32, 47

[40] Nicholas Metropolis, Arianna W Rosenbluth, Marshall N Rosenbluth, Augusta H Teller, and Edward Teller. Equation of state calculations by fast computing machines. *J. Chem. Phys.*, 21(6):1087–1092, 1953. 17

[41] D.A. McQuarrie. *Statistical Mechanics*. University Science Books, 2000. 18

[42] David Chandler. Introduction to modern statistical mechanics. *Introduction to Modern Statistical Mechanics, by David Chandler, pp. 288. Foreword by David Chandler. Oxford University Press, Sep 1987. ISBN-10: 0195042778. ISBN-13: 9780195042771*, 1, 1987. 19

[43] J. P. Hansen and I. McDonald. *Theory of Simple Liquids*. Academic, London, 1990. 20

[44] Daan Frenkel and Berend Smit. Understanding molecular simulation: from algorithms to applications. *Computational sciences series*, 1:1–638, 2002. 20

[45] J. L. Yarnell, M. J. Katz, R. G. Wenzel, and S. H. Koenig. Structure factor and radial distribution function for liquid argon at 85 °k. *Phys. Rev. A*, 7:2130–2144, Jun 1973. 21

[46] LOUP VERLET. Computer "experiments" on classical fluids. ii. equilibrium correlation functions. *Phys. Rev.*, 165:201–214, Jan 1968. 21

[47] Dominique Levesque and Loup Verlet. Note on x-ray scattering by argon. *Phys. Rev. Lett.*, 20:905–907, Apr 1968. 21

[48] David R Nelson, Michael Rubinstein, and Frans Spaepen. Order in two-dimensional binary random arrays. *Philos. Mag. A*, 46(1):105–126, 1982. 26

[49] LV Woodcock. Entropy difference between the face-centred cubic and hexagonal close-packed crystal structures. *Nature*, 385(6612):141–143, JAN 9 1997. 29

[50] Alex Soibel, Eli Zeldov, Michael Rappaport, Yuri Myasoedov, Tsuyoshi Tamegai, Shuuichi Ooi, Marcin Konczykowski, and Vadim B. Geshkenbein. Imaging the vortex-lattice melting process in the presence of disorder. *Nature*, 406(6793):282–287, 07 2000. 29

[51] P. M. Chaikin and T. C. Lubensky. *Principles of Condensed Matter Physics*. Cambridge University Press, New York, 2000. 29

[52] F. Ebert, P. Keim, and G. Maret. Local crystalline order in a 2d colloidal glass former. *Eur. Phys. J. E*, 26:161–168, 2008. 29, 40, 42, 44, 46

[53] Lahcen Assoud, Florian Ebert, Peter Keim, René Messina, Georg Maret, and Hartmut Löwen. Ultrafast quenching of binary colloidal suspensions in an

external magnetic field. *Phys. Rev. Lett.*, 102:238301, Jun 2009. 29, 44, 45, 46, 49

[54] Sven Deutschländer, Tobias Horn, Hartmut Löwen, Georg Maret, and Peter Keim. Two-dimensional melting under quenched disorder. *Phys. Rev. Lett.*, 111:098301, Aug 2013. 29, 35, 40, 41, 42

[55] P. M. Reis, R. A. Ingale, and M. D. Shattuck. Caging dynamics in a granular fluid. *Phys. Rev. Lett.*, 98:188301, Apr 2007. 29

[56] Nicolás Rivas, Suomi Ponce, Basile Gallet, Dino Risso, Rodrigo Soto, Patricio Cordero, and Nicolás Mujica. Sudden chain energy transfer events in vibrated granular media. *Phys. Rev. Lett.*, 106:088001, Feb 2011. 29

[57] Robabeh Moosavi, Maniya Maleki, M. Reza Shaebani, J. Carlos Ruiz-Suárez, and Eric Clément. Stripe formation in horizontally oscillating granular suspensions. *EPL (Europhysics Letters)*, 107(3):34006, 2014. 29

[58] S. Merminod, M. Berhanu, and E. Falcon. Transition from a dissipative to a quasi-elastic system of particles with tunable repulsive interactions. *EPL (Europhysics Letters)*, 106(4):44005, 2014. 29

[59] Gwennou Coupier. *Elasticity and pinning in macroscopic Wigner crystals : a model system for the study of weak pinning.* Theses, Université Pierre et Marie Curie - Paris VI, October 2006. 31

[60] Charles Kittel, Paul McEuen, and Paul McEuen. *Introduction to solid state physics*, volume 8. Wiley New York, 1976. 38

[61] J M Burgers. Geometrical considerations concerning the structural irregularities to be assumed in a crystal. *Proceedings of the Physical Society*, 52(1):23, 1940. 38

[62] Jooyoung Lee and Katherine J. Strandburg. First-order melting transition of the hard-disk system. *Phys. Rev. B*, 46:11190–11193, Nov 1992. 38

[63] Katherine J. Strandburg. Two-dimensional melting. *Rev. Mod. Phys.*, 60:161–207, Jan 1988. 38

[64] Hans Hennig von Grünberg, Peter Keim, and Georg Maret. Phase transitions in two-dimensional colloidal systems. 2007. 38

[65] Boris Delaunay. Sur la sphere vide. *Izv. Akad. Nauk SSSR, Otdelenie Matematicheskii i Estestvennyka Nauk*, 7(793-800):1–2, 1934. 39

[66] Atsuyuki Okabe, Barry Boots, Kokichi Sugihara, and Sung Nok Chiu. *Spatial tessellations: concepts and applications of Voronoi diagrams*, volume 501. John Wiley & Sons, 2009. 39

[67] N.W. Ashcroft and N.D. Mermin. *Solid State Physics*. Saunders College, Philadelphia, 1976. 39

[68] Paul M Chaikin and Tom C Lubensky. *Principles of condensed matter physics*, volume 1. Cambridge Univ Press, 2000. 39

[69] P. Keim, G. Maret, and H. H. von Grünberg. Frank's constant in the hexatic phase. *Phys. Rev. E*, 75:031402, Mar 2007. 40

[70] Sven Deutschländer, Antonio M. Puertas, Georg Maret, and Peter Keim. Specific heat in two-dimensional melting. *Phys. Rev. Lett.*, 113:127801, Sep 2014. 42

[71] R. Messina. Electrostatics in soft matter. *J. Phys.: Condens. Matter*, 21:113102, 2009. 44

[72] Qian Chen, Jonathan K. Whitmer, Shan Jiang, Sung Chul Bae, Erik Luijten, and Steve Granick. Supracolloidal Reaction Kinetics of Janus Spheres. *Science*, 331(6014):199–202, JAN 14 2011. 44

[73] H. Löwen, E. C. Oğuz, L. Assoud, and R. Messina. *Colloidal Crystallization Between Two and Three Dimensions*, volume 148, chapter 3, pages 225–249. John Wiley & Sons, Inc., 2012. 45

[74] Sander Pronk and Daan Frenkel. Large difference in the elastic properties of fcc and hcp hard-sphere crystals. *Physical Review Letters*, 90(25):255501, 2003. 45

[75] Hong Xu and M Baus. A density functional study of superlattice formation in binary hard-sphere mixtures. *Journal of Physics: Condensed Matter*, 4(50):L663, 1992. 45

[76] MD Eldridge, PA Madden, and D Frenkel. Entropy-driven formation of a superlattice in a hard-sphere binary mixture. *Nature*, 365(6441):35–37, 1993. 45

[77] Neil Hunt, Roger Jardine, and Paul Bartlett. Superlattice formation in mixtures of hard-sphere colloids. *Phys. Rev. E*, 62:900–913, Jul 2000. 45

[78] C. N. Likos and C. L. Henley. *Philos. Mag. B*, 68:85–86, 1993. 45

[79] L. Assoud, R. Messina, and H. Löwen. Stable crystalline lattices in two-dimensional binary mixtures of dipolar particles. *Europhys. Lett.*, 80:48001, 2007. 45, 46, 48, 49, 50, 53, 56, 61

[80] Julia Fornleitner, Federica Lo Verso, Gerhard Kahl, and Christos N. Likos. Ordering in two-dimensional dipolar mixtures. *Langmuir*, 25(14):7836–7846, 2009. 45

[81] Alexandros Chremos and Christos N. Likos. Crystal structures of two-dimensional binary mixtures of dipolar colloids in tilted external magnetic fields. *J. Phys. Chem. B*, 113(36):12316–12325, 2009. PMID: 19663484. 45, 56

[82] T. Stirner and J. Sun. Molecular dynamics simulation of the structural configuration of binary colloidal monolayers. *Langmuir*, 21:6636–6641, 2005. 45

[83] Lahcen Assoud, Florian Ebert, Peter Keim, René Messina, Georg Maret, and Hartmut Löwen. Crystal nuclei and structural correlations in two-dimensional colloidal mixtures: experiment versus simulation. *J. Phys.: Condens. Matter*, 21(46):464114, 2009. 45, 46, 49

[84] Adam D. Law, D. Martin A. Buzza, and Tommy S. Horozov. Two-dimensional colloidal alloys. *Phys. Rev. Lett.*, 106:128302, Mar 2011. 45

[85] Thierry Biben and Jean-Pierre Hansen. Phase separation of asymmetric binary hard-sphere fluids. *Phys. Rev. Lett.*, 66:2215–2218, Apr 1991. 46

[86] Daan Frenkel and Berend Smit. *Understanding molecular simulation: from algorithms to applications*. Academic press, 2001. 47

[87] VA Froltsov, R Blaak, CN Likos, and H Löwen. Crystal structures of two-dimensional magnetic colloids in tilted external magnetic fields. *Physical Review E*, 68(6):061406, 2003. 56